Dynamic electric-field-induced response of charged spherical colloids in uncharged hydrogels

MU WANG[1] AND REGHAN J. HILL[1,2] †

[1]Department of Chemical Engineering, McGill University, Montreal, Quebec H3A 2B2, Canada
[2]McGill Institute for Advanced Materials, McGill University, Montreal, Quebec H3A 2B2, Canada

Embedding colloidal particles in polymeric hydrogels often endows the polymer skeleton with appealing characteristics for microfluidics and biosensing applications. This theoretical study provides a rigorous foundation for interpreting active electrical microrheology and electroacoustic experiments on such materials. In addition to viscoelastic properties of the composites, these techniques sense physicochemical characteristics of the particle–polymer interface. Wang & Hill (*Soft Matter*, vol. 4, 2008, p. 1048) studied the steady response of a rigid, impenetrable sphere in a compressible hydrogel skeleton. Here, we extend their analysis to arbitrary frequencies, showing, in general, how the frequency response depends on the particle size and charge, ionic strength of the electrolyte and elastic and hydrodynamic characteristics of the polymer skeleton. Our calculations capture the transition from quasi-steady compressible to quasi-steady incompressible dynamics as the frequency passes through the reciprocal draining time of the gel. Above the reciprocal draining time, the skeleton and fluid move in unison, so the dynamics are incompressible and, thus, given to an excellent approximation by the well-known dynamic electrophoretic mobility but with the Newtonian shear viscosity replaced by a complex, frequency-dependent value.

---

1. Introduction

Hydrogels are an important class of soft matter that have gained widespread application in drug delivery (Peppas *et al.* 2000; Qiu & Park 2001; Lin & Netters 2006), tissue engineering (Drury & Mooney 2003; Barndl, Sommer & Goepferich 2007; Khademhosseini & Langer 2007), advanced materials (Eddington & Beebe 2004; Peppas *et al.* 2006; Chaterji, Kwon & Park 2007) and molecular separations (Wang, Burban & Cussler 1993; Kim & Park 1998). Novel characteristics can be achieved by immobilizing organic and inorganic colloidal particulates in the polymer skeleton. For example, embedding gold or gold-coated silica nanoparticles into a thermally responsive hydrogel induces light-wavelength-sensitive swelling to achieve optically active microfluidic flow control (Sershen *et al.* 2005). In biosensing, immobilizing silica nanoparticles in polyacrylamide hydrogels and applying an electric field increase the otherwise diffusion-limited flux of uncharged macromolecules across the composite membrane (Matos, White & Tilton 2006). This flux enhancement can be attributed to electro-osmotic flow (Hill 2006*b*), and theoretical predictions

† Email address for correspondence: reghan.hill@mcgill.ca

from continuum electrokinetic theory are in good agreement with the available experiments (Hill 2007). Other applications include delivering growth factors for bone regeneration (Chung *et al.* 2007), improving the contrast of ultrasound imaging for early tumour detection (Dayton & Ferrara 2002; Liu *et al.* 2006) and absorbing infrared energy for certain cancer treatment (Loo *et al.* 2005). Note also that polystyrene nanoparticles have been dispersed in neutral polyacrylamide hydrogels to increase the storage modulus and produce mechanoelectrical effects for artificial tactile perception and psychosensorial materials (Thévenot *et al.* 2007).

Advances in the development and application of hydrogel–colloid composites could benefit from a quantitative characterization of the microstructure. This motivates the present theoretical study, where we investigate the response of hydrogel–colloid composites to dynamic electric fields. Our theory provides a first step towards quantifying the electrical, hydrodynamic and mechanical interactions under dynamic conditions. It therefore establishes a rigorous foundation for interpreting electrical microrheology and electroacoustic experiments. We show that electrophoretic microrheology (Mizuno, Kimura & Hayakawa 2000; Kimura & Mizuno 2007) is appropriate at low frequencies, whereas the response to electric fields at high frequencies is best probed using electroacoustics, namely the electrokinetic sonic amplitude (ESA; O'Brien 1988, 1990; Hunter 1998).

In microrheology, the storage and loss moduli of soft materials, such as hydrogels and polymer solutions, can be obtained from the frequency-dependent susceptibility of probe particles in an external field (Ziemann, Radler & Sackmann 1994; Breuer 2005). One advantage of applying a dynamic electric field is that the viscoelastic properties of the matrix and the physicochemical characteristics of the probe particles could be simultaneously measured using knowledge of the amplitude and phase of the response. Note that physicochemical properties, such as the surface charge or ζ-potential of the inclusions, are important for electro-osmotic pumping (Yao *et al.* 2003; Yao & Santiago 2003; Matos *et al.* 2006; Hill 2007) and micromixing (Matos, White & Tilton 2008). Another advantage of dynamic experiments is that the spectral response provides considerably more information than a steady experiment (Russel, Schowalter & Saville 1989; Hunter 2001).

Microrheology is often adopted for materials that are too fragile for bulk rheology measurements (MacKintosh & Schmidt 1999; Breuer 2005; Cicuta & Donald 2007). Passive microrheology, such as diffusing wave spectroscopy (Pine *et al.* 1988; Mason & Weitz 1995) or one- and two-particle microrheology (Crocker, Valentine & Weeks 2000; Levine & Lubensky 2000), measures thermal fluctuations in the displacement of probe particles. In active microrheology, the probe particles typically respond to applied magnetic (Ziemann *et al.* 1994) or optical (Valentine, Dewalt & Ou-Yang 1996; Yamaguchi *et al.* 2005) forces.

Mizuno *et al.* (2000), Mizuno, Kimura & Hayakawa (2001, 2004) and Kimura & Mizuno (2007) have applied electric fields in a novel heterodyne light scattering technique to measure the dynamic electrophoretic mobility of nanoparticles in dilute lamellar phases. Their experiments simultaneously measure the dynamic mobility and diffusion coefficient of probe particles at frequencies from less than 1 Hz to about 50 kHz. Microrheology techniques can also be applied to assess the surface characteristics of colloidal particles. With optical tweezers, Galneder *et al.* (2001) measured the ζ-potential of phospholipid-bilayer-coated silica beads by monitoring electrophoretic forces. Electrical microrheology could also be applied to hydrogel–colloid composites, perhaps allowing simultaneous characterization of the viscoelastic and physicochemical properties of the composite microstructure.

The upper frequency limit of electrical microrheology is about 50 kHz (Mizuno *et al.* 2000). Higher frequencies have been achieved with Newtonian colloidal dispersions using electroacoustics, typically operating between 0.3 and 11 MHz (Hunter 1998). Electroacoustics has also been successful for determining the size and ζ-potential of colloidal particles in Newtonian electrolytes. It includes the colloid vibration potential, arising from external sound waves, and the ESA, generated by oscillating electric fields. These techniques are independent of the suspension optical properties and are therefore particularly well suited for opaque and concentrated dispersions. Modern electroacoustic theories (O'Brien 1988, 1990) connect the macroscopic electric-field-induced pressure disturbances or sound-wave-generated electrical potentials to the dynamic mobility and polarizability of dispersed colloidal particles. Theoretical calculations of the dynamic electrophoretic mobility for dilute (O'Brien 1988; Mangelsdorf & White 1992; Preston, Kornbrekke & White 2005) and concentrated (Rider & O'Brien 1993; O'Brien, Jones & Rowlands 2003; Ahualli *et al.* 2006) suspensions have been successfully compared with experiments (Hunter 1998).

In this work, we connect the macroscopic electroacoustic response of hydrogel–colloid composites to the dynamic electrophoretic mobility of a single colloidal particle embedded in a hydrogel matrix. In particular, we show that the electroacoustic response is proportional to the mobility (velocity) of colloidal particles in hydrogels. Accordingly, our analysis demonstrates that the electroacoustic response of a hydrogel–colloid composite could be measured using electroacoustic instruments currently available for colloidal dispersions. More importantly, we identify the frequency range in which the electroacoustic signal is particularly sensitive to the elasticity of the hydrogel skeleton. This could facilitate novel experiments to monitor the kinetics of gelation and other developments of the microstructure (Sato & Breedveld 2006; Larsen & Furst 2008). Noteworthy is that the dynamic electrophoretic mobility at megahertz frequencies is particularly high for relatively stiff polymer skeletons, whereas the displacement response at such frequencies is vanishingly small and, therefore, beyond the detection limit of particle-tracking microrheology instruments.

Previous theories for the steady electric-field-induced displacement of spherical colloidal particles in uncharged hydrogels (Hill & Ostoja-Starzewski 2008; Wang & Hill 2008) reveal that the colloid displacement reflects a simple balance between the electrical Coulomb force and the elastic restoring force of the gel when the particle radius a is much smaller than the Debye screening length κ^{-1}. This situation prevails with small particles and low electrolyte concentrations. Otherwise, when $\kappa a \gg 1$, the displacement quantifies how electro-osmotic flow, arising from the diffuse layer of counterions that envelops each inclusion, interacts with the polymer skeleton. The latter is considerably more challenging to compute but is analytically tractable.

Wang & Hill (2008) recently showed that compressibility of the hydrogel skeleton, as quantified by Poisson's ratio ν, can have a significant influence on the particle displacement Z when a charged inclusion is subjected to a steady electric field E. When $\kappa a \gg 1$ and $\ell \ll a$, for example,

$$Z/E = 2\epsilon_o\epsilon_s\zeta\mathscr{E}^{-1}(1+\nu) + \frac{\epsilon_o\epsilon_s\zeta\kappa a(1+\nu)(1-2\nu)}{2\mathscr{E}(\kappa\ell+1)(1-\nu)}, \tag{1.1}$$

where ζ is the well-known ζ-potential; $\mathscr{E}$ and ℓ are Young's modulus and Brinkman screening length (Brinkman 1947) of the polymer skeleton (ℓ^2 is the Darcy permeability); and ϵ_o and ϵ_s are the vacuum permittivity and dielectric constant of the hydrogel. For an incompressible skeleton ($\nu = 0.5$), the second term on the right-hand side of (1.1) vanishes and the displacement is independent of the particle size. For

compressible skeletons with $\nu \sim 0.2$, however, the displacement increases linearly with κa. Therefore, in the experimentally accessible parameter space, the particle displacement in compressible hydrogels can be an order of magnitude larger than in incompressible hydrogels.

Note that the apparent compressibility of a hydrogel depends on the draining time (Schnurr *et al.* 1997; Hill & Ostoja-Starzewski 2008)

$$\tau_d \sim (1 - 2\nu)(\eta/\mathscr{E})(a/\ell)^2, \tag{1.2}$$

where η is the fluid viscosity. If the experimental time scale $\tau_c < \tau_d$, the fluid is unable to escape the polymer network, so the hydrogel deforms in an incompressible manner; otherwise, the skeleton has time to drain and adopt its equilibrium (compressible) state of strain. Consistent with scaling theory (Geissler & Hecht 1980, 1981), the Poisson ratio of hydrogel skeletons is generally found to be in the range 0–0.25, so the draining time is indeed finite.

In addition to the draining time, other important time scales affect the response. For example, balancing the $O(\eta u^* a^{-1})$ viscous hydrodynamic stresses with the $O(\mu u^* \tau_v a^{-1})$ elastic elastic stresses identifies a viscoelastic time scale $\tau_v = \eta \mu^{-1}$. Here, u^* is the characteristic velocity and μ is the shear modulus of the polymer skeleton. Moreover, balancing the $O(\rho_f u^* \tau_f^{-1})$ inertial stresses with the foregoing viscous stresses identifies an intrinsic fluid time scale $\tau_f = a^2 \rho_f \eta^{-1}$, where ρ_f is the fluid density. At frequencies greater than the reciprocal viscoelastic time scale, the dynamics are the same as in the absence of polymer; i.e. at high enough frequencies the dynamic mobility of an inclusion in a hydrogel becomes equal to its mobility in a Newtonian electrolyte. Note that the ion diffusion time $\tau_i = (a + \kappa^{-1})^2 D^{-1}$ (DeLacey & White 1981), where D is a characteristic ion diffusivity, provides a time scale for accessing dynamics of polarization and relaxation of the diffuse double layer, but this has a relatively weak influence on particle dynamics. Although the foregoing time scales are helpful for understanding qualitative aspects of the dynamics, quantitative transitions between these characteristic times must be established by calculating the frequency spectrum of the colloid displacement.

In this work, frequency spectra are calculated from an electrokinetic model with the fluid and hydrogel skeleton coupled by Darcy drag. When electrical forces are negligible, i.e. in the absence of an electric field and surface charge, the hydrodynamic and elastic equations of motion couple, yielding a so-called two-fluid model. This provides the response function for probe particles subjected to a known external force. Levine & Lubensky (2001) derived an approximate response function that neglects fluid inertia, which is reasonable at frequencies below several kilohertz. However, much higher frequencies are important for electrophoretic microrheology and electroacoustics. Therefore, to correctly interpret such experiments, an exact solution of the full two-fluid model is required. An exact solution of this model is also necessary for calculating the dynamic electric-field-induced response. More specifically, the two-fluid model provides far-field boundary conditions for accurately calculating the electric-field-induced particle response, which is governed by the much more complex multi-phase electrokinetic model addressed in this work.

This paper is arranged in three parts. The first part (§ 2) solves the two-fluid model analytically for an uncharged spherical colloid in a compressible, uncharged hydrogel. After presenting the model and its solution, we compare the results with the approximation of Levine & Lubensky (2001), the generalized Stokes–Einstein relation (GSER) and the well-known solution of the unsteady Stokes equations. The

second part (§ 3) addresses the full multi-phase electrokinetic model. After presenting the governing equations and boundary conditions, the forces on the particle are expressed in terms of asymptotic coefficients that reflect far-field decays of several disturbances to the equilibrium state. In turn, these are used to calculate the dynamic electric-field-induced particle displacement from the particle equation of motion. We then turn to the results, examining dynamic response spectra at frequencies from the low-frequency compressible steady limit to well beyond the ultrasonic range. The third part (§ 4) studies an important application of the multi-phase electrokinetic model to electroacoustic diagnostics. Following O'Brien (1988, 1990), we establish the link between the electroacoustic response of dilute hydrogel–colloid composite and the single-particle dynamic electrophoretic mobility. An analytical boundary-layer analysis, valid for high frequencies, is undertaken. This permits a comparison of numerically exact and analytical approximate calculations of the dynamic electrophoretic mobility, focusing on how the elasticity of the polymer gel distinguishes particle dynamics from those already established for colloids dispersed in Newtonian electrolytes. Section 5 provides a concluding summary.

2. Two-fluid model and response function (dynamic susceptibility) for uncharged spheres

2.1. *Governing equations and boundary conditions*

Consider an uncharged spherical colloid with radius a and density ρ_p embedded in an uncharged hydrogel with Young's modulus $\mathscr{E}$, Poisson's ratio ν and Darcy permeability ℓ^2. The particle is subjected to a harmonically oscillating external force $\boldsymbol{F}\exp(-\mathrm{i}\omega t)$, where ω is the angular frequency and $\mathrm{i}=\sqrt{-1}$. In microrheology, such a force arises from optical or magnetic fields, which are generally decoupled from the fluid and polymer. The particle responds by undergoing a displacement $\boldsymbol{Z}\exp(-\mathrm{i}\omega t)$ that reflects the hydrodynamic and elastic forces as determined from the fluid velocity $\boldsymbol{u}$ and polymer displacement $\boldsymbol{v}$. Accordingly, the response function

$$\alpha(\omega) \equiv Z/F \qquad (2.1)$$

is obtained by satisfying the particle equation of motion.

In the absence of electrical influences, the two-fluid model in the frequency domain for harmonic dynamics comprises (e.g. Levine & Lubensky 2001)

$$-\mathrm{i}\omega\rho_f\boldsymbol{u} = -\nabla p + \eta\nabla^2\boldsymbol{u} - \eta\ell^{-2}(\boldsymbol{u} + \mathrm{i}\omega\boldsymbol{v}), \qquad (2.2a)$$

$$0 = \nabla\cdot\boldsymbol{u}, \qquad (2.2b)$$

$$0 = \mu\nabla^2\boldsymbol{v} + (\mu + \lambda)\nabla(\nabla\cdot\boldsymbol{v}) + \eta\ell^{-2}(\boldsymbol{u} + \mathrm{i}\omega\boldsymbol{v}), \qquad (2.2c)$$

where p is the pressure, and the first and second Lamé constants, λ and μ respectively, are related to Young's modulus $\mathscr{E}$ and Poisson's ratio ν by $\lambda = \mathscr{E}\nu/[(1+\nu)(1-2\nu)]$ and $\mu = \mathscr{E}/[2(1+\nu)]$. In a frame of reference that moves with the sphere, the boundary conditions are $\boldsymbol{u}=\boldsymbol{v}=0$ at $r=a$ and $\boldsymbol{u}\to-\mathrm{i}\omega\boldsymbol{Y}$, $\boldsymbol{v}\to\boldsymbol{Y}$ as $r\to\infty$, where $\boldsymbol{Y}=-\boldsymbol{Z}$.

In general, the first and second Lamé constants for the polymer skeleton are complex and frequency dependent (Larson 1999). However, their determination requires specific knowledge of the polymer architecture and gelation. Therefore, for simplicity, the first and second Lamé constants are specified here to be real constants. Note that time derivatives appear via the factor $-\mathrm{i}\omega$; polymer inertia is neglected because of its low concentration; and the fluid and polymer are coupled by the Darcy drag force $\eta\ell^{-2}(\boldsymbol{u} + \mathrm{i}\omega\boldsymbol{v})$.

2.2. *Fluid velocity and polymer displacement fields*

Following Markov (2005), we construct the fluid velocity and polymer displacement fields as

$$\boldsymbol{u} = \nabla\varPhi_1 + \nabla \times \boldsymbol{\Psi}_1 + \nabla \times \boldsymbol{\Psi}_2 - \mathrm{i}\omega\boldsymbol{Y}, \tag{2.3a}$$

$$\boldsymbol{v} = m\nabla\varPhi_1 + \nabla\varPhi_2 + M_1\nabla \times \boldsymbol{\Psi}_1 + M_2\nabla \times \boldsymbol{\Psi}_2 + \boldsymbol{Y}, \tag{2.3b}$$

where $\varPhi_1$ and $\varPhi_2$ are scalar functions; $\boldsymbol{\Psi}_1$ and $\boldsymbol{\Psi}_2$ are vector functions; and m, M_1 and M_2 are constants. Physically, $\varPhi_1$ can be attributed to the pressure in the incompressible fluid; $\varPhi_2$ represents a compressional wave; and $\boldsymbol{\Psi}_1$ and $\boldsymbol{\Psi}_2$ represent shear waves.

Fluid incompressibility (2.2b) requires

$$\nabla^2\varPhi_1 = 0, \tag{2.4}$$

so taking the divergence of (2.2c) and substituting (2.3a) and (2.3b) gives

$$\nabla^2[\nabla^2(m\varPhi_1 + \varPhi_2) + \eta\ell^{-2}(\lambda + 2\mu)^{-1}\varPhi_1 + \mathrm{i}\omega\eta\ell^{-2}(\lambda + 2\mu)^{-1}(m\varPhi_1 + \varPhi_2)] = 0. \tag{2.5}$$

Next, eliminating $\varPhi_1$ by setting $m = -(\mathrm{i}\omega)^{-1}$ gives

$$\nabla^2\varPhi_2 + k^2\varPhi_2 = 0, \tag{2.6}$$

where

$$k^2 = \mathrm{i}\omega\eta\ell^{-2}(\mu + 2\lambda)^{-1}. \tag{2.7}$$

Taking the curl of (2.2a) and (2.2c) and substituting (2.3a) and (2.3b) gives

$$\nabla \times \nabla \times \sum_{j=1}^{2}[\eta\nabla^2 + (\mathrm{i}\omega\rho_f - \eta\ell^{-2} - \mathrm{i}\omega\eta\ell^{-2}M_j)]\boldsymbol{\Psi}_j = 0, \tag{2.8a}$$

$$\nabla \times \nabla \times \sum_{j=1}^{2}[\mu M_j\nabla^2 + (\eta\ell^{-2} + \mathrm{i}\omega\eta\ell^{-2}M_j)]\boldsymbol{\Psi}_j = 0, \tag{2.8b}$$

which can be written

$$\nabla^2\boldsymbol{\Psi}_j + K_j^2\boldsymbol{\Psi}_j = 0 \ (j = 1, 2), \tag{2.9}$$

where

$$K_j^2 = (\mathrm{i}\omega\rho_f - \eta\ell^{-2} - \mathrm{i}\omega\eta\ell^{-2}M_j)/\eta \ (j = 1, 2). \tag{2.10}$$

For $\boldsymbol{\Psi}_1$ and $\boldsymbol{\Psi}_2$ to be distinct, M_1 and M_2 must be roots of the quadratic

$$\mathrm{i}\omega\mu\ell^{-2}M_j^2 + [\mathrm{i}\omega\eta\ell^{-2} + \mu\ell^{-2} - \mathrm{i}\omega\rho_f(\mu/\eta)]M_j + \eta\ell^{-2} = 0. \tag{2.11}$$

The wavenumbers k correspond to the propagation of compressional waves, and K_1 and K_2 are associated with shear waves. Note that all the foregoing wavenumbers can also be obtained from the Fourier representation of the governing equations (Levine & Lubensky 2001).

With the prevailing axisymmetric spherical geometry, the Laplace equation (2.4) and Helmholtz equations (2.6) and (2.9) are easily solved analytically. The vector potential $\boldsymbol{\Psi}_j$ can be written $\boldsymbol{\Psi}_j = \Psi_j\boldsymbol{e}_\phi$ $(j = 1,2)$ (Lamb 1945; Oestreicher 1951; Temkin & Leung 1976; Markov 2005), where $\boldsymbol{e}_\phi$ is one of the mutually orthogonal unit basis vectors $(\boldsymbol{e}_r, \boldsymbol{e}_\theta, \boldsymbol{e}_\phi)$ for spherical polar coordinates (r, θ, ϕ) with respect to the polar axis $\boldsymbol{e}_z$ such that $\boldsymbol{e}_z \cdot \boldsymbol{e}_r = \cos\theta$. Since the fluid velocity and polymer

displacement must be linear with respect to Y and vanish as $r \to \infty$, we have

$$\Phi_1 = A_1 r^{-2} Y \cos\theta, \qquad (2.12a)$$

$$\Phi_2 = A_2 h(kr) Y \cos\theta, \qquad (2.12b)$$

$$\Psi_j = B_j h(K_j r) Y \sin\theta \ (j = 1, 2), \qquad (2.12c)$$

where $h(x) = -x^{-2}(x + \mathrm{i}) \exp(\mathrm{i}x)$ is the spherical Hankel function of the first kind, which represents an outward-propagating wave, and A_j and B_j ($j = 1, 2$) are constants to satisfy the boundary conditions at $r = a$. To ensure vanishing far-field disturbances, $\mathrm{Im}(k) > 0$, $\mathrm{Im}(K_1) > 0$ and $\mathrm{Im}(K_2) > 0$.

The radial and tangential components of the fluid velocity and polymer displacement are

$$u_r = \left[-2A_1 r^{-3} + 2\sum_{j=1}^{2} B_j r^{-1} h(K_j r) - \mathrm{i}\omega \right] Y \cos\theta, \qquad (2.13a)$$

$$u_\theta = \left\{ A_1 r^{-3} + \sum_{j=1}^{2} B_j K_j [(K_j r)^{-1} h(K_j r) + h'(K_j r)] - \mathrm{i}\omega \right\}(-Y \sin\theta), \qquad (2.13b)$$

$$v_r = \left[-2m A_1 r^{-3} + A_2 k h'(kr) + 2\sum_{j=1}^{2} M_j B_j r^{-1} h(K_j r) + 1 \right] Y \cos\theta, \qquad (2.13c)$$

$$v_\theta = \left\{ m A_1 r^{-3} + A_2 r^{-1} h(kr) + \sum_{j=1}^{2} M_j B_j K_j [(K_j r)^{-1} h(K_j r) + h'(K_j r)] + 1 \right\}$$
$$\times (-Y \sin\theta). \qquad (2.13d)$$

Note that the prime on the spherical Hankel function denotes its first derivative, and the constants A_j and B_j ($j = 1, 2$) are chosen to satisfy the no-slip boundary conditions at $r = a$.

2.3. *Force and response function*

The force exerted on the sphere by the fluid and polymer is calculated from knowledge of the fluid velocity and polymer displacement. Integrating the hydrodynamic and elastic surface tractions over the particle surface (Landau & Lifshitz 1987) gives a force (magnitude)

$$F = (4/3)\pi a^2 [-\mathrm{i}\omega\rho_f A_1 Y/a^2 + (\mathrm{i}\omega\eta\ell^{-2} - \lambda k^2) A_2 Y h(ka) + 2f_1(a) + 2f_2(a)]$$
$$= -4\pi \mathrm{i}\omega\rho_f A_1 Y, \qquad (2.14a)$$

where

$$f_1(r) \cos\theta = \eta u_{r,r} + \mu v_{r,r}, \qquad (2.14b)$$

$$f_2(r) \sin\theta = \eta u_{\theta,r} + \mu v_{\theta,r}. \qquad (2.14c)$$

Note that the subscript 'r' following commas denotes differentiation with respect to r. Equation (2.14a) is also obtained by applying Gauss's divergence theorem to the volume enclosed by the particle surface and a large concentric sphere. With no-slip boundary conditions at $r = a$,

$$A_1 = a^3 (\Theta + \Gamma)(2H)^{-1}, \qquad (2.15a)$$

where

$$\Theta = \omega(M_1 - M_2)\big[2\mathrm{i}(\beta_1\beta_2)^2(b + \mathrm{i}) - 2b^2(\beta_1 + \mathrm{i})(\beta_2 + \mathrm{i})$$
$$+ b^2(\beta_1^2 + \mathrm{i}\beta_1 - 1)(\beta_2^2 + \mathrm{i}\beta_2 - 1)\big], \tag{2.15b}$$

$$\Gamma = 2(b^2 + 3\mathrm{i}b - 3)\big[\beta_1^2(1 + \mathrm{i}\omega M_1)(\beta_2 + \mathrm{i}) - \beta_2^2(1 + \mathrm{i}\omega M_2)(\beta_1 + \mathrm{i})\big], \tag{2.15c}$$

$$H = \mathrm{i}(\beta_1\beta_2)^2(b^2 + 2\mathrm{i}b - 2)(M_1 - M_2)$$
$$+ b^2\big[\beta_1^2(M_2 - m)(\beta_2 + \mathrm{i}) - \beta_2^2(M_1 - m)(\beta_1 + \mathrm{i})\big], \tag{2.15d}$$

with $b = ka$ and $\beta_j = K_j a$ $(j = 1, 2)$.

Finally, in a stationary reference frame, also accounting for particle and fluid inertia (Appendix D), the particle equation of motion is

$$\boldsymbol{F} + 4\pi\mathrm{i}\omega\rho_f A_1 \boldsymbol{Z} = \omega^2 V_p(\rho_f - \rho_p)\boldsymbol{Z}, \tag{2.16}$$

where $V_p = (4/3)\pi a^3$ is the particle volume, and recall $\boldsymbol{Z} = -\boldsymbol{Y}$. Our exact solution of the two-fluid model for the response function (dynamic susceptibility) is therefore

$$\alpha(\omega) = [\omega^2 V_p(\rho_f - \rho_p) - 4\pi\mathrm{i}\omega\rho_f A_1]^{-1}. \tag{2.17}$$

To evaluate A_1 in (2.17), quadratic equation (2.11) is solved for M_1 and M_2, which provide wavenumbers K_1 and K_2 from (2.10). Next, k is obtained from (2.7). Note that $\mathrm{Im}(k) > 0$ and $\mathrm{Im}(K_j) > 0$ $(j = 1, 2)$. After evaluating b, β_1 and β_2, (2.15b)–(2.15d) give Θ, Γ and H, which provide A_1 from (2.15a). Several of the foregoing steps must be performed using multiple precision algebra (Enge, Pélissier & Zimmermann 2007; Fousse *et al.* 2007; Granlund 2007). The integrals in the approximation of Levine & Lubensky (2001) are easily evaluated using standard numerical quadrature.

2.4. *Comparison of analytical exact and approximate solutions*

The dynamic susceptibility $\alpha(\omega)$ for an uncharged particle is shown in figure 1. Our exact analytical solution (2.17) is compared with the approximation of Levine & Lubensky (2001) and the GSER where $\alpha(\omega) = [6\pi a(\mu - \mathrm{i}\omega\eta)]^{-1}$. The figure also highlights several reciprocal time scales identified in the introduction. Note that $\omega_B = \eta^{-1}(2\mu + \lambda)(\ell/a)^2(\pi^2/4)$; ω^* satisfies $|\beta(\omega^*)| = 1$, where $\beta(\omega) = 4a^2\omega^2\rho_f/[(\mu - \mathrm{i}\omega\eta)\pi^2]$; $\omega_d = 2\pi(1 - 2\nu)^{-1}(\mathscr{E}/\eta)(\ell/a)^2$; and $\omega_v = 2\pi\mu/\eta$. The first two of these were adopted by Levine & Lubensky (2001): ω_B is identified as the network compression frequency above which the elastic network is hydrodynamically coupled with the incompressible fluid, and ω^* is the frequency above which fluid inertia dominates the response. The other two reciprocal time scales, ω_d and ω_v, are, respectively, proportional to the reciprocal draining time and reciprocal fluid time (§ 1). The results with Brinkman screening length $\ell = 1$ and $100\,\mathrm{nm}$ are representative of tightly and loosely coupled fluid and polymer. Other parameters are summarized in table 1. Recall that the first and second Lamé constants (μ and λ) of the hydrogel skeleton are real constants here.

The transition from quasi-steady compressible to incompressible dynamics is evident from the plateau seen in figure 1(*a*) at intermediate frequencies with $\ell = 1\,\mathrm{nm}$. When $\ell = 100\,\mathrm{nm}$, however, $\tau_d \sim \tau_v$, so the low-frequency plateau (compressible elastic regime) in figure 1(*c*) transits to the high-frequency viscous dominated regime without an intermediate (incompressible elastic) plateau.

The real parts of the quasi-steady compressible and quasi-steady incompressible elastic plateaus differ by at most 25 %, as predicted by Schnurr *et al.* (1997). This relatively small change is often used to justify neglecting compressibility when interpreting optical and magnetic tweezers microrheology experiments (Ziemann *et al.*

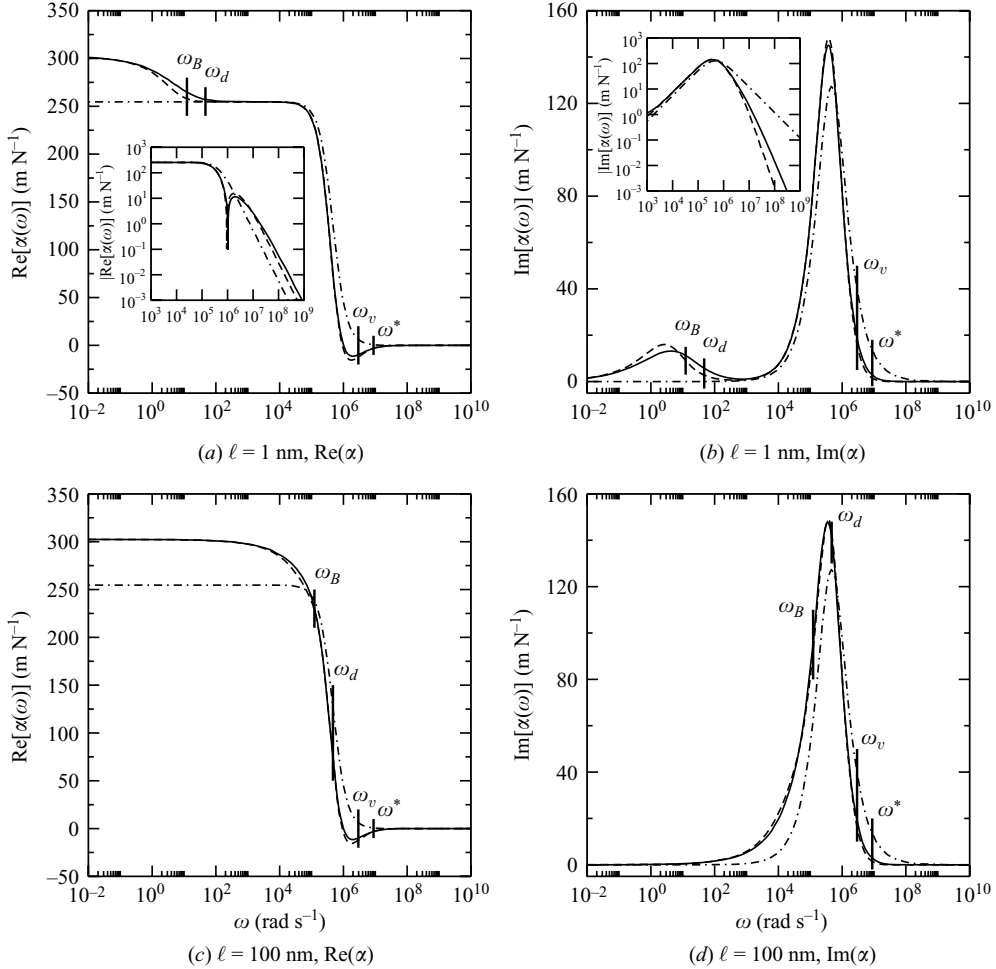|	
Particle radius a	500 nm
Fluid viscosity η	8.904×10^{-4} Pa s
Polymer Young's modulus $\mathscr{E}$	1 kPa
Polymer Poisson's ratio ν	0.2
Fluid density ρ_f	997 kg m^{-3}
Particle density ρ_p	2000 kg m^{-3}

TABLE 1. Parameters for the results shown in figure 1.

FIGURE 1. Response function $\alpha(\omega)$ as a function of angular frequency ω for different Brinkman screening lengths: (a, b) $\ell = 1$ nm and (c, d) $\ell = 100$ nm. Other parameters are listed in table 1. The solid lines are exact solutions of the two-fluid model (2.17); the dashed lines are the approximation of Levine & Lubensky (2001); and the dash-dotted lines are the GSER. Several characteristic frequencies are identified (see the text for details): $\omega_v \approx 2.9 \times 10^6$ rad s^{-1} and $\omega^* \approx 8.8 \times 10^6$ rad s^{-1} for all panels; (a, b) $\omega_B \approx 12$ rad s^{-1}, $\omega_d \approx 47$ rad s^{-1}; and (c, d) $\omega_B \approx 1.23 \times 10^5$ rad s^{-1}, $\omega_d \approx 4.70 \times 10^5$ rad s^{-1}. Equation (2.18) (not shown for clarity) recovers the GSER (dash-dotted lines) when $\omega \lesssim \omega_d$ and recovers the exact solution (solid lines) when $\omega \gtrsim \omega_d$.

1994; Schnurr *et al.* 1997). However, if the external force is accompanied by electro-osmotic flow, compressibility is much more significant when $\kappa a \gtrsim 1$ (Wang & Hill 2008). This regime is explored in the sections below, where we address the dynamic electric-field-induced response.

The approximation of Levine and Lubensky is valid when fluid inertia can be neglected. Accordingly, it agrees well with our exact solution when $\omega \ll \omega^*$. As highlighted in the insets of figures 1(*a*) and 1(*b*), which have logarithmic axes, the theory of Levine and Lubensky yields increasingly large relative errors at higher frequencies. However, the absolute displacement is practically zero at such high frequencies, so the errors are of minor concern for magnetic and optical microrheology, but have important consequences for electroacoustics.

To capture particle and fluid inertia for incompressible skeletons at any frequency, we note that the solution of the unsteady Stokes equations (Landau & Lifshitz 1987), with the Newtonian shear viscosity η replaced by a complex shear viscosity $\eta^* = \eta + i\mu\omega^{-1}$, gives (Berg-Sørensen & Flyvbjerg 2004; Mizuno *et al.* 2008)

$$\alpha^{-1} = -i\omega 6\pi\eta^* a(1 + a/\delta) - \omega^2[3\pi a^2\delta\rho_f + (4/3)\pi a^3\rho_p(1 + 0.5\rho_f/\rho_p)], \qquad (2.18)$$

where $\delta = [2\eta^*/(\rho_f\omega)]^{1/2}$. This connection to the unsteady Stokes equations arises when there is zero relative motion of the fluid and polymer skeleton, i.e. $\boldsymbol{u} = -i\omega\boldsymbol{v}$, which is realized at all frequencies when the polymer is incompressible and has zero inertia. One can then add the fluid and polymer equations of motion to yield the unsteady Stokes equations with shear viscosity η^*. As expected, (2.18) agrees with our (2.17) (solid lines in figure 1) at frequencies above the reciprocal draining time and with the GSER (dash-dotted lines in figure 1) at frequencies below the reciprocal draining time.

Our exact solution (2.17) of the two-fluid model – valid for compressible skeletons at all frequencies – is required to solve the full multi-phase electrokinetic model. As described in Appendix B, the two-fluid model provides far-field boundary conditions for the fluid velocity and polymer displacement fields; it also provides the basis of an analytical approximation for the high frequencies encountered in electroacoustics.

3. Multi-phase electrokinetic model and electric-field-induced response

In general, the particle surface charge is screened by a diffuse layer of electrolyte ions and counterions, whose bulk concentration determines the Debye length κ^{-1} and surface potential ζ for a given surface charge density σ. However, when $\kappa a \ll 1$, the external force on the particle equals the bare Coulomb force $\boldsymbol{F} = \sigma 4\pi a^2 \boldsymbol{E}$, and there is vanishing electro-osmotic flow. Therefore, the ratio of the particle displacement to the electric field strength under these conditions is simply

$$Z/E = \sigma 4\pi a^2 \alpha(\omega). \qquad (3.1)$$

Hydrogel compressibility affects Z/E by at most 25 %, which is evident from scaling analysis (Schnurr *et al.* 1997) and the approximate response function of Levine & Lubensky (2001). When $\kappa a \gtrsim 1$, however, an electrokinetic model is necessary to capture the influence of electro-osmotic flow and polarization of the diffuse double layer, which together modify the phase and amplitude of the effective Coulomb force on the particle. Electrical influences may also impart a so-called electroviscous resistance to particle dynamics, so, in general, $\alpha(\omega)$ above also depends on the particle charge and electrolyte concentration.

3.1. *Model equations and boundary conditions*

Our multi-phase electrokinetic model augments the two-fluid model in §2 with an electrical body force on the fluid, a Poisson equation linking the electrostatic potential to the free-charge density and electrolyte-ion conservation equations to account for ion diffusion, electromigration and convection. With harmonic time dependence, e.g. an applied electric field $E \exp(-i\omega t)$, the full electrokinetic model is

$$0 = \epsilon_o \epsilon_s \nabla^2 \psi + \sum_{j=1}^{N} n_j z_j e, \quad (3.2a)$$

$$-i\omega n_j = -\nabla \cdot \boldsymbol{j}_j, \quad (3.2b)$$

$$-i\omega \rho_f \boldsymbol{u} = \eta \nabla^2 \boldsymbol{u} - \nabla p - \eta \ell^{-2}(\boldsymbol{u} + i\omega \boldsymbol{v}) - \sum_{j=1}^{N} n_j z_j e \nabla \psi, \quad (3.2c)$$

$$0 = \nabla \cdot \boldsymbol{u}, \quad (3.2d)$$

$$0 = \mu \nabla^2 \boldsymbol{v} + (\lambda + \mu)\nabla(\nabla \cdot \boldsymbol{v}) + \eta \ell^{-2}(\boldsymbol{u} + i\omega \boldsymbol{v}), \quad (3.2e)$$

with ion fluxes

$$\boldsymbol{j}_j = n_j \boldsymbol{u} - D_j \nabla n_j - z_j e n_j D_j (kT)^{-1} \nabla \psi. \quad (3.2f)$$

Note that ψ is the electrostatic potential and n_j is the concentration of the jth ion species with valence z_j and diffusivity D_j. The fundamental charge and thermal energy are e and kT, respectively, and the diffusivities of the N ion species are related to their limiting conductances Λ_j (Speight 2005) by $D_j = (kT\Lambda_j)/(e^2|z_j|)$. Note that the Debye length is $\kappa^{-1} = \sqrt{kT\epsilon_s\epsilon_o/(2Ie^2)}$, where the ionic strength $I = (1/2)\sum_{j=1}^{N} z_j^2 n_j^\infty$ with n_j^∞ the bulk concentration of the jth ion species.

Among the principal assumptions underlying this model are a linearly elastic hydrogel skeleton that is isotropic and homogeneous (Hill & Ostoja-Starzewski 2008) and does not hinder ion diffusion and electromigration (Hill 2006b). Furthermore, the colloidal particle is assumed to be rigid, and displacement and velocity fields are assumed to be continuous across the particle–hydrogel interface. As suggested by mode-coupling theory for charged colloidal dispersions (Nägele 2003), a continuum theory may be too crude an approximation for particles smaller than the polymer mesh length. Moreover, polymer depletion or concentration at the particle–polymer interface will modulate the effective elastic properties of the skeleton, thereby changing the amplitude and phase of the response. Such influences have been considered by Levine & Lubensky (2000) for the purely mechanical response but are beyond the scope of the present study addressing the electrical response.

In a reference frame moving with the particle, no-slip boundary conditions at the particle surface require $\boldsymbol{u} = \boldsymbol{v} = 0$ at $r = a$. Other possibilities such as slipping or the opening of a crack at the particle–hydrogel interface significantly complicate the problem and are not pursued here. An impenetrable and non-conducting particle demands $\psi_> = \psi_<$, $\epsilon_p \epsilon_o (\boldsymbol{e}_r \cdot \nabla_<)\psi - \epsilon_s \epsilon_o (\boldsymbol{e}_r \cdot \nabla_>)\psi = \sigma$ and $\boldsymbol{j}_j \cdot \boldsymbol{e}_r = 0$, where ϵ_p is the particle dielectric constant, $\boldsymbol{e}_r$ is the outward unit normal and the subscripts '<' and '>' distinguish the particle and hydrogel sides of the interface, respectively.

Far from the particle, disturbances to the equilibrium electrostatic potential, ion concentrations, fluid velocity and polymer displacement vanish. Therefore, as $r \to \infty$, $\psi \to -\boldsymbol{E} \cdot \boldsymbol{r}$, $n_j \to n_j^\infty$, $\boldsymbol{u} \to i\omega \boldsymbol{Z}$ and $\boldsymbol{v} \to -\boldsymbol{Z}$. Note that these boundary conditions cannot be directly applied in numerical computations because the slowly

decaying, oscillating disturbances yield numerical instabilities. We remedy this with the asymptotic analysis detailed in Appendix B.

3.2. *Solution methodology*

The equations above are solved by linearizing perturbations from an equilibrium base state governed by the nonlinear Poisson–Boltzmann equation. This methodology is widely adopted for calculating the steady and dynamic electrophoretic mobilities of colloidal particles (O'Brien & White 1978; Mangelsdorf & White 1992; Hill, Saville & Russel 2003*a*) and a variety of other electrokinetic phenomena. The perturbation approach is accurate when the applied electric field is sufficiently weak, i.e. $|\mathbf{E}| \ll \kappa\zeta$. Under these conditions, which are often achieved in experiments, the methodology is much more computationally efficient than solving the full nonlinear model (Masliyah & Bhattacharjee 2006).

The equilibrium base state (ψ^0 and n_j^0) prevails in the absence of external stimuli. In this work, perturbations to equilibrium are induced by a far-field translation of the hydrogel $\mathbf{Y} = -\mathbf{Z}$ and external electric field $\mathbf{E}$. Accordingly, ψ and n_j are constructed as $\psi = \psi^0 + \psi' = \psi^0 - \mathbf{E}\cdot\mathbf{r} + \psi''$ and and $n_j = n_j^0 + n_j'$, where linearity and axisymmetry demand $n_j' = \hat{n}_j(r)\mathbf{X}\cdot\mathbf{e}_r$ and $\psi'' = \hat{\psi}(r)\mathbf{X}\cdot\mathbf{e}_r$, with $\mathbf{X} \in \{\mathbf{Y}, \mathbf{E}\}$. Note that fluid velocity $\mathbf{u}$ and polymer displacement $\mathbf{v}$ are perturbed quantities whose constructions are given below. It is expedient to linearize the perturbations and construct the solution by superposing two sub-problems with either $\mathbf{Y} = 0$ or $\mathbf{E} = 0$ and the particle fixed at the origin.

As is well known, the equilibrium ion concentrations are $n_j^0 = n_j^\infty \exp[-z_j e\psi^0/(kT)]$, and the Poisson–Boltzmann equation with spherical symmetry is

$$\epsilon_o\epsilon_s\mathscr{L}_0\psi^0 = -\sum_{j=1}^{N} z_j n_j^0 e, \tag{3.3}$$

with boundary conditions $\psi^0 = \zeta$ or $\epsilon_s\epsilon_o\psi_{,r}^0 = -\sigma$ at $r = a$ and $\psi^0 \to 0$ as $r \to \infty$. We solve (3.3) using a standard finite-difference method with an adaptive grid (Hill *et al.* 2003*a*) that ensures ψ^0 decays as $\exp(-r)/r$ when $\kappa(r - a) \gg 1$ (Verwey & Overbeek 1948; Shkel, Tsodikov & Record Jr 2000).

Following our earlier work (Wang & Hill 2008), the fluid velocity and compressible polymer displacement are constructed as

$$\mathbf{u} = \nabla \times \nabla \times [f(r)\mathbf{X}] - i\omega\mathbf{Y}$$
$$= -i\omega\mathbf{Y} + (-r^{-1}f_{,r} - f_{,rr})\mathbf{X} + (-r^{-1}f_{,r} + f_{,rr})\mathbf{X}\cdot\mathbf{e}_r\mathbf{e}_r, \tag{3.4}$$
$$\mathbf{v} = g_1(r)\mathbf{X} + g_2(r)\mathbf{X}\cdot\mathbf{e}_r\mathbf{e}_r + \mathbf{Y}, \tag{3.5}$$

so taking the curl of the fluid momentum equation (3.2*c*) gives

$$-i\omega\rho_f\mathscr{L}_1 f_{,r} = \eta\mathscr{L}_2 f_{,rrr} - \eta\ell^{-2}[\mathscr{L}_1 f_{,r} - i\omega(g_{1,r} - r^{-1}g_2)]$$
$$- \sum_{j=1}^{N} z_j e r^{-1}\{\hat{n}_j\psi_{,r}^0 - n_{j,r}^0[\hat{\psi} - r(E/X)]\}, \tag{3.6}$$

where

$$\mathscr{L}_0(\cdot) = (\cdot)_{,rr} + 2r^{-1}(\cdot)_{,r}, \tag{3.7a}$$
$$\mathscr{L}_1(\cdot) = (\cdot)_{,rr} + 2r^{-1}(\cdot)_{,r} - 2r^{-2}(\cdot), \tag{3.7b}$$
$$\mathscr{L}_2(\cdot) = (\cdot)_{,rr} + 4r^{-1}(\cdot)_{,r} - 4r^{-2}(\cdot). \tag{3.7c}$$

The X and $X \cdot e_r e_r$ components of the polymer momentum equation (3.2e) are

$$0 = \mu(g_{1,rr} + 2r^{-1}g_{1,r} + 2r^{-2}g_2) + (\mu + \lambda)(r^{-1}g_{1,r} + r^{-1}g_{2,r} + 2r^{-2}g_2)$$
$$+ \eta\ell^{-2}(-f_{,rr} - r^{-1}f_{,r} + i\omega g_1), \tag{3.8}$$

$$0 = \mu(g_{2,rr} + 2r^{-1}g_{2,r} - 6r^{-2}g_2) + (\mu + \lambda)(g_{1,rr} + g_{2,rr} - r^{-1}g_{1,r} + r^{-1}g_{2,r} - 4r^{-2}g_2)$$
$$+ \eta\ell^{-2}(f_{,rr} - r^{-1}f_{,r} + i\omega g_2), \tag{3.9}$$

and the perturbed Poisson equation (3.2a) and ion-conservation equations (3.2b) are

$$\epsilon_o \epsilon_s \mathscr{L}_1 \hat{\psi} = -\sum_{j=1}^{N} z_j \hat{n}_j e, \tag{3.10}$$

$$-i\omega \hat{n}_j = n_{j,r}^0 [2r^{-1}f_{,r} + i\omega(Y/X)] + D_j \mathscr{L}_1 \hat{n}_j + z_j e D_j (kT)^{-1}$$
$$\times \{n_{j,r}^0 [\hat{\psi}_{,r} - (E/X)] + \psi_{,r}^0 \hat{n}_{j,r} + n_j^0 \mathscr{L}_1 \hat{\psi} + \hat{n}_j \mathscr{L}_0 \psi^0\}. \tag{3.11}$$

The boundary conditions for $\hat{\psi}$ and $\hat{n}_j$ at $r = a$ are

$$\hat{\psi}_{,r} - (E/X) - (\epsilon_p/\epsilon_s)[\hat{\psi}/a - (E/X)] = 0, \tag{3.12a}$$

$$z_j e D_j (kT)^{-1}\{\hat{n}_j \psi_{,r}^0 + n_j^0 [\hat{\psi}_{,r} - (E/X)]\} + D_j \hat{n}_{j,r} = 0, \tag{3.12b}$$

and no slip at $r = a$ requires

$$f_{,r} = -(i\omega a/2)(Y/X) \quad \text{and} \quad f_{,rr} = -(i\omega/2)(Y/X), \tag{3.12c}$$

$$g_1 = -(Y/X) \quad \text{and} \quad g_2 = 0. \tag{3.12d}$$

Finally, vanishing of the disturbances as $r \to \infty$ requires

$$\hat{\psi} \to 0 \quad \text{and} \quad \hat{n}_j \to 0, \tag{3.13a}$$

$$f_{,r} \to 0 \quad \text{and} \quad f_{,rr} \to 0, \tag{3.13b}$$

$$g_1 \to 0 \quad \text{and} \quad g_2 \to 0. \tag{3.13c}$$

3.3. *Forces and dynamic electrical response*

The force and particle response are written in terms of asymptotic coefficients that characterize the far-field decays of the fluid velocity and polymer displacement. Since the electrical body force vanishes as $r \to \infty$,

$$u^X \to -i\omega Y + C^X r^{-3} X - 3C^X r^{-3} X \cdot e_r e_r, \tag{3.14a}$$

$$v^X \to Y + Z^X r^{-3} X - 3Z^X r^{-3} X \cdot e_r e_r, \tag{3.14b}$$

where $X \in \{E, Y\}$. Recall that (3.14a) and (3.14b) emerge from the two-fluid model presented in §2. Since the fluid and polymer skeleton move together in the far field, their respective asymptotic coefficients C^X and Z^X are related by $Z^X = -(i\omega)^{-1} C^X$. Accordingly, the force and particle displacement can be written in terms of C^X alone.

Electrical, hydrodynamic and elastic forces are exerted on the particle in the E and Y sub-problems. The corresponding stress tensors are the Maxwell stress

$$T^m = \epsilon_o \epsilon_s \nabla\psi\nabla\psi - (1/2)\epsilon_o \epsilon_s (\nabla\psi \cdot \nabla\psi)I, \tag{3.15}$$

Newtonian hydrodynamic stress

$$T^f = -pI + \eta[\nabla u + (\nabla u)^T] \tag{3.16}$$

and linear elastic stress

$$T^e = \lambda(\nabla \cdot v)I + \mu[\nabla v + (\nabla v)^T], \tag{3.17}$$

where I is the identity tensor.

The total force is

$$\boldsymbol{F}^X = \int_{r=a} (\boldsymbol{T}^m + \boldsymbol{T}^f + \boldsymbol{T}^e) \cdot \boldsymbol{e}_r \, \mathrm{d}A, \tag{3.18}$$

so applying Gauss's divergence theorem to a volume that encloses the particle surface and a large concentric sphere with radius $r \to \infty$ gives

$$\boldsymbol{F}^X = \int_{r\to\infty} (\boldsymbol{T}^m + \boldsymbol{T}^f + \boldsymbol{T}^e) \cdot \boldsymbol{e}_r \, \mathrm{d}A - \int_{r=a}^{r\to\infty} \nabla\cdot(\boldsymbol{T}^m + \boldsymbol{T}^f + \boldsymbol{T}^e)\,\mathrm{d}V, \tag{3.19}$$

where

$$\nabla \cdot \boldsymbol{T}^m = -\rho^e \nabla\psi, \tag{3.20a}$$
$$\nabla \cdot \boldsymbol{T}^f = -\mathrm{i}\omega\rho_f \boldsymbol{u} + \eta\ell^{-2}(\boldsymbol{u} + \mathrm{i}\omega\boldsymbol{v}) + \rho^e \nabla\psi, \tag{3.20b}$$
$$\nabla \cdot \boldsymbol{T}^e = -\eta\ell^{-2}(\boldsymbol{u} + \mathrm{i}\omega\boldsymbol{v}), \tag{3.20c}$$

and $\rho^e = \sum_{j=1}^{N} n_j z_j e$ is the free-charge density. Accordingly, the force is

$$\begin{aligned}
\boldsymbol{F}^X &= \int_{r\to\infty} (\boldsymbol{T}^m + \boldsymbol{T}^f + \boldsymbol{T}^e) \cdot \boldsymbol{e}_r \, \mathrm{d}A + \mathrm{i}\omega\rho_f \int_{r=a}^{r\to\infty} \boldsymbol{u}\,\mathrm{d}V \\
&= \int_{r\to\infty} (\boldsymbol{T}^m + \boldsymbol{T}^f + \boldsymbol{T}^e) \cdot \boldsymbol{e}_r \, \mathrm{d}A \\
&\quad + \mathrm{i}\omega\rho_f \left[\int_{r\to\infty} (\boldsymbol{u}\cdot\boldsymbol{e}_r)\boldsymbol{r}\,\mathrm{d}A - \int_{r=a} (\boldsymbol{u}\cdot\boldsymbol{e}_r)\boldsymbol{r}\,\mathrm{d}A \right].
\end{aligned} \tag{3.21}$$

Note that the first integral on the left-hand side of (3.21) is finite only if the stress decays as r^{-2}. The only such term involves the fluid pressure, so with the no-slip boundary conditions at $r = a$ we find

$$\boldsymbol{F}^X = -\int_{r\to\infty} p\boldsymbol{e}_r \, \mathrm{d}A + \mathrm{i}\omega\rho_f \int_{r\to\infty} (\boldsymbol{u}\cdot\boldsymbol{e}_r)\boldsymbol{r}\,\mathrm{d}A. \tag{3.22}$$

Substituting the velocity from (3.14a) into the second integral on the right-hand side of (3.22) gives

$$\int_{r\to\infty} (\boldsymbol{u}\cdot\boldsymbol{e}_r)\boldsymbol{r}\,\mathrm{d}A = -(8/3)\pi C^X \boldsymbol{X} - \mathrm{i}\omega \int_{r\to\infty} (\boldsymbol{Y}\cdot\boldsymbol{e}_r)\boldsymbol{r}\,\mathrm{d}A, \tag{3.23}$$

and as $r \to \infty$,

$$p \to \int^{r} [\eta\nabla^2\boldsymbol{u} + \mathrm{i}\omega\rho_f \boldsymbol{u} - \eta\ell^{-2}(\boldsymbol{u} + \mathrm{i}\omega\boldsymbol{v}) - \rho^e \nabla\psi] \cdot \boldsymbol{e}_r\,\mathrm{d}r'. \tag{3.24}$$

Since $\nabla^2\boldsymbol{u} \sim r^{-5}$ and $\rho^e \nabla\psi$ decays exponentially, the r^{-2} decaying and growing contributions give

$$\begin{aligned}
p &= [\mathrm{i}\omega\rho_f C^X r^{-2} - \eta\ell^{-2}(C^X + \mathrm{i}\omega Z^X)r^{-2}](\boldsymbol{X}\cdot\boldsymbol{e}_r) + \omega^2\rho_f r(\boldsymbol{Y}\cdot\boldsymbol{e}_r) \\
&= \mathrm{i}\omega\rho_f C^X r^{-2}(\boldsymbol{X}\cdot\boldsymbol{e}_r) + \omega^2\rho_f r(\boldsymbol{Y}\cdot\boldsymbol{e}_r),
\end{aligned} \tag{3.25}$$

and finally, the force on the particle is

$$\boldsymbol{F}^X = -4\pi\mathrm{i}\omega\rho_f C^X \boldsymbol{X}. \tag{3.26}$$

Note that the radially growing term in (3.25) cancels the surface integral on the right-hand side of (3.23) when evaluating the force. Equation (3.26) has the same form as for a Newtonian fluid and is valid for both compressible and incompressible polymer skeletons.

Time scale		Value (s)
Draining	$\tau_d \sim (\eta/\mathscr{E})(a/\ell)^2$	$\sim 10^{-2}$
Ion diffusion	$\tau_i \sim a^2/D_j$	$\sim 10^{-3}$
Viscoelastic	$\tau_v \sim \eta/\mu$	$\sim 10^{-6}$
Fluid (momentum diffusion)	$\tau_f \sim \rho_f a^2/\eta$	$\sim 10^{-6}$

TABLE 2. Summary of the characteristic time scales (reciprocal frequencies) used to interpret the spectral response functions. Representative values are listed for the dimensional parameters: $a \sim 1\,\mu\text{m}$, $\ell \sim 10\,\text{nm}$, $\mathscr{E} \sim \mu = 1\,\text{kPa}$, $\rho_f \sim 10^3\,\text{kg m}^{-3}$, $\eta \sim 10^{-3}\,\text{Pa s}$, $D_j \sim 10^{-9}\,\text{m}^2\,\text{s}^{-1}$. At frequencies below (above) τ_d^{-1} the hydrogel responds in a compressible (incompressible) manner; and at frequencies below (above) τ_v^{-1} the particle dynamics reflects the hydrogel elasticity (viscosity). See the text for other details.

Superposing the $\boldsymbol{E}$ and $\boldsymbol{Y}$ problems with $\boldsymbol{Y} = -\boldsymbol{Z}$ and correctly accounting for fluid and particle inertia (Appendix D) give

$$-4\pi\mathrm{i}\omega\rho_f C^E \boldsymbol{E} + 4\pi\mathrm{i}\omega\rho_f C^Y \boldsymbol{Z} = \omega^2 V_p \boldsymbol{Z}(\rho_f - \rho_p), \qquad (3.27)$$

where $V_p = (4/3)\pi a^3$ is the particle volume. Accordingly, the dynamic electric-field-induced response is

$$Z/E = \mathrm{i}C^E/[\mathrm{i}C^Y + \omega a^3(\rho_p - \rho_f)/(3\rho_f)]. \qquad (3.28)$$

3.4. *Numerical solutions of the full electrokinetic model*

The electrokinetic model is solved numerically by adopting κ^{-1}, $u^* = \epsilon_s\epsilon_o(kT/e)^2/(\eta a)$ and $\eta u^*/\mu = \epsilon_s\epsilon_o(kT/e)^2/(\mu a)$ as the characteristic scales for length, fluid velocity and polymer displacement, respectively; and similar to (3.28), the dimensional response Z/E is obtained from the dimensionless asymptotic coefficients $\hat{C}^E$ and $\hat{C}^Y$ as

$$Z/E = \frac{\mathrm{i}\hat{C}^E \epsilon_o\epsilon_s(kT/e)/(\mu\kappa a)}{\mathrm{i}\hat{C}^Y - (\omega\eta/\mu)(\kappa a)^3(\rho_f - \rho_p)/(3\rho_f)}. \qquad (3.29)$$

Separate computer programs were written to calculate the response for compressible and incompressible hydrogels. Asymptotic coefficients are extracted from the far-field decay of the perturbations, and the dynamic response Z/E is obtained from the superposition leading to (3.28) or (3.29). Note that the asymptotic analysis detailed in Appendix B provides Z/E at frequencies from as low as 0.01 Hz to higher than 1 GHz. An algorithmic description of the computational methodologies and external libraries used in our programs is provided in Appendix E.

For a given electrolyte, a dimensionless response Z^* can be written in terms of six principal independent dimensionless parameters:

$$\mathscr{E}eZ/(E\epsilon_o\epsilon_s kT) = Z^*[\zeta e/(kT), \kappa a, \kappa\ell, \omega\eta/\mathscr{E}, \rho_f\mathscr{E}a^2/\eta^2, \rho_p/\rho_f]. \qquad (3.30)$$

The last three dimensionless arguments arise from the dynamics; i.e. the steady response is independent of these dimensionless groups. Nevertheless, to maintain a close connection to experiments, we present the results in dimensional form. It follows, for example, that the dimensional displacement Z is inversely proportional to Young's modulus $\mathscr{E}$ at low frequencies. In particular, we discuss the results in terms of the characteristic time scales discussed in the introduction. For convenient reference, these are summarized in table 2 with their representative order of magnitude for a specific set of representative dimensional variables. Note that Young's modulus $\mathscr{E}$, Brinkman
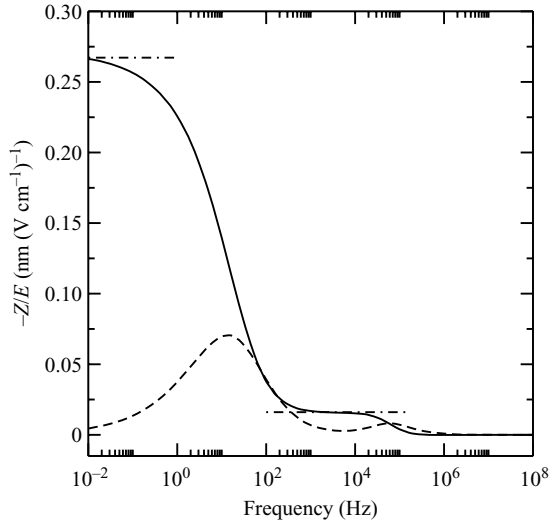
FIGURE 2. Representative frequency spectrum of Z/E for a charged colloidal sphere embedded in an uncharged, compressible electrolyte-saturated hydrogel: NaCl at $T = 298$ K; $a = 500$ nm; $\kappa a = 500$; $-\zeta e/(kT) = 3$; $\ell = 5$ nm; $\rho_p = 1050$ kg m^{-3}, $\nu = 0.2$; and $\mathscr{E} = 800$ Pa. The solid and dashed lines are the real and imaginary parts of Z/E from numerical solutions of the full multi-phase electrokinetic model; and the dash-dotted lines are the formula of Wang & Hill (2008) (1.1) with $\nu = 0.2$ and $\nu = 0.5$.

screening length ℓ and particle size a can vary by several orders of magnitude, imparting equally significant changes in the time scales and, thus, the spectral response.

A representative spectrum of Z/E for a colloidal particle in a compressible hydrogel is presented in figure 2. The computations are validated, in part, by the steady boundary-layer formula (1.1) for compressible and incompressible hydrogels (Hill & Ostoja-Starzewski 2008; Wang & Hill 2008). Note that the response (real part) undergoes a distinct transition from quasi-steady compressible to quasi-steady incompressible elastic plateaus as the frequency passes through the reciprocal draining time $\tau_d^{-1} \approx 150$ Hz. The transition spans several frequency decades, with the steady compressible asymptote realized at extremely low frequencies $\sim 10^{-2}$ Hz. Note that the small discrepancy between the steady (horizontal line) and low-frequency dynamic asymptote in figure 2 is due to the boundary-layer approximation (1.1), which, in this example, is about 2 % smaller than the numerically exact result (Wang & Hill 2008).

The quasi-steady compressible and incompressible elastic responses differ by an order of magnitude here. At higher frequencies, $|Z/E|$ becomes vanishingly small because the viscous and inertial stresses dominate the response. Note that in active microrheology, most experimentally accessible frequencies are in transition from the quasi-steady compressible to incompressible elastic regimes, so the dynamic calculations are essential for correctly interpreting such experiments. For the hydrogel–colloid composite in figure 2, an applied electric field $E = 20$ V cm^{-1} with frequency $\omega/(2\pi) = 1$ Hz induces a particle displacement with amplitude $Z \approx 4$ nm that could be resolved using back-focal-plane interferometry (Allersma *et al.* 1998). The sub-nanometre displacements at higher frequencies ($\gtrsim 10$ kHz) could be detected by correlating the oscillatory forcing and response using a lock-in amplifier (e.g. Mizuno *et al.* 2008). At ultrasonic frequencies, the particle velocity $-i\omega Z$ in response to an oscillatory electric field can be measured using electroacoustics (e.g. O'Brien 1988).
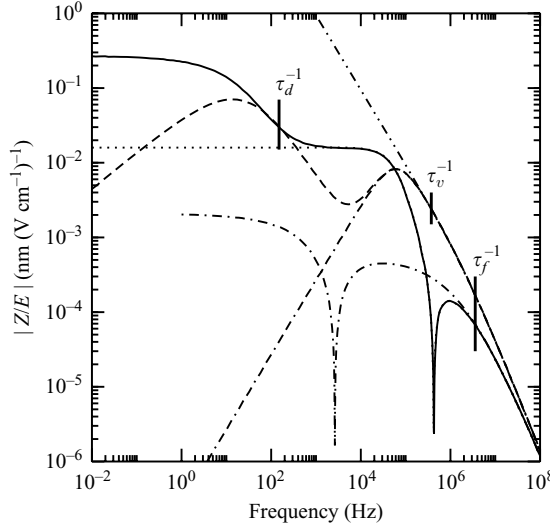
FIGURE 3. Comparison of Z/E for a compressible hydrogel with the response $(Z/E)^* = \mu_d^* \mathrm{i}\omega^{-1}$ for incompressible dispersions. The parameters are the same as in figure 2. The solid and dashed lines are the real and imaginary parts of Z/E from numerical solutions of the full multi-phase electrokinetic model. The dash-dotted and dash-double-dotted lines are the real and imaginary parts of $(Z/E)^*$ calculated from the MPEK software package for a Newtonian electrolyte (Hill *et al.* 2003a). The dotted and dot-double-dashed lines are the real and imaginary parts of $(Z/E)^*$ from O'Brien's dynamic electrophoretic mobility formula (3.31) evaluated with a complex viscosity $\eta^* = \eta + \mathrm{i}\mu\omega^{-1}$.

The high-frequency regime is examined in figure 3, where the absolute values of the real and imaginary parts of Z/E for particles in a hydrogel (solid and dashed lines) are compared with their counterparts $(Z/E)^* = \mu_d^* \mathrm{i}\omega^{-1}$ for the same particles dispersed in the electrolyte without polymer. Accordingly, quantities with the superscripts '*' are from numerical solutions of the standard electrokinetic model (Mangelsdorf & White 1992), including particle and fluid inertia at any frequency (Hill, Saville & Russel 2003b), as calculated by the MPEK software package (Hill *et al.* 2003a). Also shown in the figure are the real and imaginary parts of $(Z/E)^*$ from O'Brien's dynamic electrophoretic mobility formula, valid at high frequencies with $\kappa a \gg 1$ (O'Brien 1988):

$$\mu_d^* = \frac{2\epsilon_s \epsilon_o \zeta}{3\eta}(1 + f)G(\omega a^2 \rho_f/\eta). \tag{3.31}$$

Note that we have evaluated (3.31) by replacing the Newtonian fluid viscosity η with a complex shear viscosity $\eta^* = \eta + \mathrm{i}\mu\omega^{-1}$. The functions f (frequency-dependent electrostatic dipole strength) and $G(\omega a^2 \rho^f/\eta)$ in (3.31) are available in O'Brien (1988).

Important characteristic frequencies in §1, including the reciprocal draining time τ_d^{-1}, reciprocal viscoelastic time τ_v^{-1} and reciprocal fluid time τ_f^{-1}, are identified in figure 3. Again, the transition from quasi-steady compressible to quasi-steady incompressible elastic dynamics is clearly evident as the frequency passes through $\tau_d^{-1} \approx 150\,\mathrm{Hz}$. More importantly, the figure highlights the transition from quasi-steady elastic to viscous dynamics as the frequency passes through $\tau_v^{-1} \approx 370\,\mathrm{kHz}$. At frequencies beyond $\tau_f^{-1} \approx 3.6\,\mathrm{MHz}$, both the real and imaginary parts of Z/E equal their $(Z/E)^*$ counterparts. Therefore, it is only at megahertz frequencies here
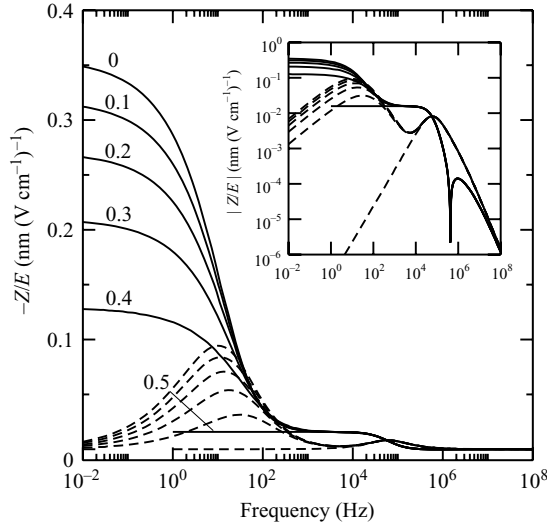
FIGURE 4. Frequency spectra of Z/E for various Poisson ratios $\nu = 0$, 0.1, 0.2, 0.3, 0.4 and 0.5 with a fixed shear modulus $\mu = 0.5\mathscr{E}/(1 + \nu) \approx 333$ Pa. All other parameters are the same as in figure 2. The solid and dashed lines are the real and imaginary parts of Z/E from numerical solutions of the full multi-phase electrokinetic model.

that the electroacoustic response of the hydrogel composite is the same as for its respective colloidal dispersion (Hunter 1998; O'Brien 1988). At lower frequencies, the electroacoustic response probes the shear modulus of the polymer skeleton and the size and charge of the inclusions.

O'Brien's formula (3.31) is valid for thin double layers and high frequencies. Under these conditions, it agrees with numerical solutions of the standard electrokinetic model. As expected, the frequency response obtained from the dynamic electrophoretic mobility with viscosity η agrees with our full multi-phase electrokinetic model at frequencies above the reciprocal viscoelastic time τ_v^{-1}. In this regime, the fluid stresses are $O(\omega\eta\mu^{-1})$ greater than the elastic stresses, so the response becomes independent of the polymer shear modulus μ. Noteworthy is that replacing the fluid viscosity η in the standard electrokinetic model (evaluated using O'Brien's formula here) with complex viscosity η^* extends the frequency range down to the reciprocal draining time τ_d^{-1} when $\tau_d^{-1} < \tau_v^{-1}$. Accordingly, the electrophoretic mobility evaluated with a complex viscosity provides an excellent approximation under conditions at which the fluid and polymer are tightly coupled. This is not the case for compressible skeletons at frequencies below τ_d^{-1}, however. For example, when $\kappa a \gg 1$ and $\ell \ll a$, evaluating the particle displacement using the steady electrical force (Wang & Hill 2008)

$$\boldsymbol{F}^E = \pi a \zeta \epsilon_o \epsilon_s \boldsymbol{E} \frac{4(1 - \nu)(\kappa\ell + 1) + (1 - 2\nu)}{(5/6 - \nu)(\kappa\ell + 1)} \tag{3.32}$$

and the dynamic susceptibility $\alpha(\omega)$ provided in §2 yields an ostensibly incorrect response at any finite frequency. In general, this is because the electrical force $\boldsymbol{F}^E$ is sensitive to the dynamic electro-osmotic flow and polarization. Note also that $\alpha(\omega)$ from §2 does not include electroviscous effects, which contribute to $\boldsymbol{F}^Z$ in the electrokinetic model.

Having identified several qualitative features of a typical frequency spectrum, let us now explore the parameter space. First, figure 4 shows how Poisson's ratio, increasing from $\nu = 0$ to $\nu = 0.5$ with fixed shear modulus $\mu \approx 0.333$ kPa, affects the response.
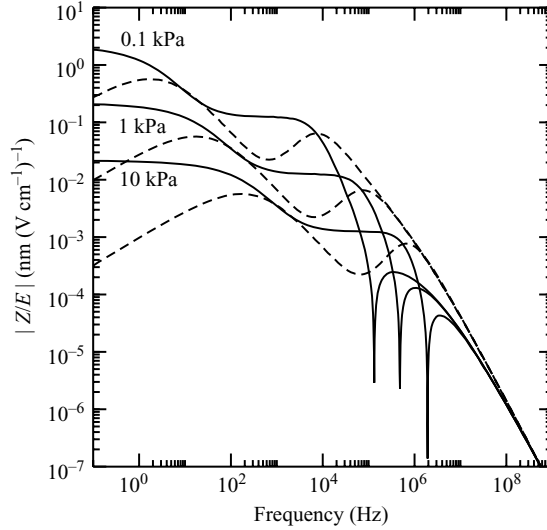
FIGURE 5. Frequency spectra of Z/E for various Young's moduli $\mathscr{E} = 0.1$, 1 and 10 kPa with Poisson ratio $\nu = 0.2$. All other parameters are the same as in figure 2. The solid and dashed lines are the real and imaginary parts of Z/E from numerical solutions of the full multi-phase electrokinetic model.

Note that the spectrum for the incompressible hydrogel ($\nu = 0.5$) was calculated using the methodology detailed in Appendix A. Comparing the spectra for $\nu = 0.5$ and $\nu < 0.5$ provides an important consistency check of our numerics, since the methodologies for compressible and incompressible skeletons are independent. In general, Z/E can vary with Poisson's ratio by up to an order of magnitude at frequencies below the reciprocal draining time. At these frequencies, the response is very sensitive to Poisson's ratio as $\nu \rightarrow 0.5$. At higher frequencies, however, Z/E is independent of Poisson's ratio with fixed shear modulus μ because the compressible skeleton is hydrodynamically coupled with the incompressible fluid.

Next, figure 5 shows how Young's modulus affects the response spectrum. As expected from the steady displacement (Hill & Ostoja-Starzewski 2008; Wang & Hill 2008), the response is indeed inversely proportional to the elastic modulus at frequencies below the reciprocal viscoelastic time τ_v^{-1}. In addition, the elastic modulus changes both the draining and viscoelastic times. Accordingly, the spectra in figure 5 overlap at frequencies below τ_v^{-1} when multiplying Z/E by $\mathscr{E}$ and dividing the frequency by $\mathscr{E}$. Noteworthy from the perspective of electroacoustics is that the real part of Z/E (solid lines) is sensitive to $\mathscr{E}$ at ultrasonic frequencies, whereas the imaginary part (dashed lines) is practically independent of $\mathscr{E}$.

The influences of the scaled ζ-potential $\zeta e/(kT)$ and scaled reciprocal double-layer thickness κa on Z/E are examined in figure 6. Note that our computational methodology is stable and accurate for all $\kappa a \gtrsim 1$. When $\kappa a \lesssim 1$, however, electro-osmotic flow is extremely weak, so the dynamic response can be approximated by (3.1). Situations of practical significance most often occur when $\kappa a \gtrsim 1$, so figure 6 presents spectra for six values of κa in the range 1–500. When κa is large, electro-osmotic flow influences the particle displacement in the quasi-steady compressible elastic regime in the same manner as for steady electric fields (Wang & Hill 2008). Consequently, the displacement at frequencies below the reciprocal draining time increases with κa relative to the respective incompressible elastic plateaus.
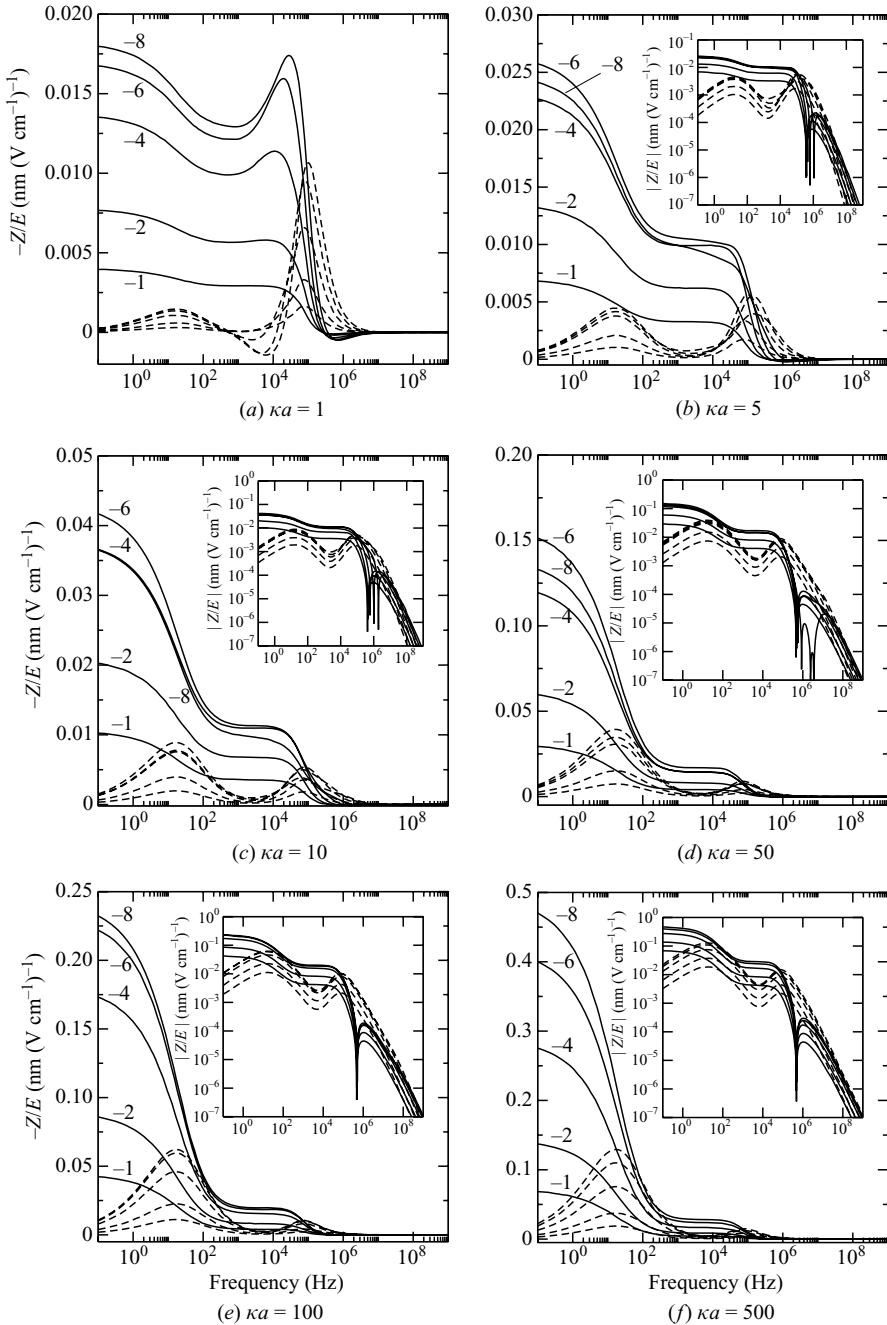
FIGURE 6. Frequency spectra of Z/E for various scaled ζ-potentials $-\zeta e/(kT) = 1, 2, 4, 6$ and 8; and various scaled reciprocal double-layer thicknesses $\kappa a = 1, 5, 10, 50, 100$ and 500: KCl at $T = 298$ K; $a/\ell = 100$ ($a = 500$ nm and $\ell = 5$ nm); $\rho_p = 1050$ kg m^{-3}; $\nu = 0.2$; and $\mathscr{E} = 1$ kPa. The solid and dashed lines are the real and imaginary parts of Z/E from numerical solutions of the full multi-phase electrokinetic model.

The response Z/E is also affected by polarization and relaxation of the diffuse double layer. This is especially evident for particles with thick double layers and high ζ-potentials, a situation in which the back-field of the polarized double layer

is strong (Gibb & Hunter 2000). For example, in figure 6(a) with $\kappa a = 1$ and $|\zeta| \gtrsim 2kT/e$, the real part of Z/E increases with frequency, and the imaginary part changes sign between approximately 2 and 30 kHz. These changes occur at frequencies above the reciprocal ion diffusion relaxation time τ_i^{-1}, which represents the maximum frequency that the diffuse double layer is capable of following the external field (DeLacey & White 1981). The increase in the real part of Z/E indicates that the back-field decreases with increasing frequency, thereby reducing the so-called retardation experienced by the particle.

The sign change of the imaginary part of Z/E indicates that the double-layer polarization lags the applied field when the frequency is above τ_i^{-1}. For particles with $\kappa a \gg 1$, the back-field is weak, because relaxation via diffusion across a thin double layer is fast. In the panels with $\kappa a = 5$, 10 and 50 in figure 6, maxima in the real part of Z/E with respect to $|\zeta|$ are evident. These can lead to ambiguity in determining the ζ-potential from the steady response (Hill & Ostoja-Starzewski 2008; Wang & Hill 2008). However, by measuring the frequency spectrum of Z/E (or the mobility $\mu_d = -\mathrm{i}\omega Z/E$), it may be easier to unambiguously ascertain the correct ζ-potential. This approach has been useful for interpreting electroacoustic measurements of the dynamic mobility (Hunter & O'Brien 1997).

Finally, figures 7 and 8, respectively, show the influence of hydrogel permeability ℓ^2 for small and large values of κa. The Brinkman screening length ℓ has a significant influence on the hydrodynamic coupling between the fluid and polymer skeleton. Earlier studies (Hill & Ostoja-Starzewski 2008; Wang & Hill 2008) have demonstrated that the polymer displacement at steady state is practically independent of ℓ for incompressible hydrogels but varies significantly for compressible hydrogels due to an adverse electro-osmotic-flow-induced pressure gradient, particularly when $\kappa a \gg 1$. Note that the Brinkman screening length also affects the draining time.

When $\kappa a \gtrsim 1$ (figure 7), the Brinkman screening length ℓ is most effective in changing the reciprocal draining time τ_d^{-1}. Accordingly, as ℓ increases, the frequency range exhibiting a quasi-steady incompressible elastic response decreases, and eventually disappears, with Z/E transferring directly from the quasi-steady compressible plateau to the viscous-stress- and inertial-stress-dominated regimes. When $\kappa a \gg 1$ (figure 8), ℓ significantly changes the amplitude of the quasi-steady compressible plateau. Similar to the steady displacement (Hill & Ostoja-Starzewski 2008; Wang & Hill 2008), decreasing the permeability increases the magnitude of the adverse tangential pressure gradient, which, in turn, increases the particle displacement.

4. Electroacoustics and dynamic electrophoretic mobility

4.1. *Electroacoustic reciprocal relation*

Here we establish the connection between the electroacoustic properties of hydrogel–colloid composites and the dynamic electric-field-induced response of a single particle addressed in § 3. Following O'Brien (1988, 1990), our analysis is applicable for composites with arbitrary particle concentration. The macroscopic momentum, mass and charge conservation equations and suspension constitutive equations from O'Brien (1990) can be directly applied to hydrogel–colloid composites, since the elasticity of the polymer does not invalidate the macroscopic equations. However, the validity of the electroacoustic reciprocal relation needs to be reviewed because of hydrogel viscoelasticity. Comparing (A7) in O'Brien (1990) with (4.3) here, we see that elastic stresses produce an additional term in the integral for deriving the reciprocal relation. With a reciprocal relation, the governing equations given by O'Brien (1990) are significantly simplified.
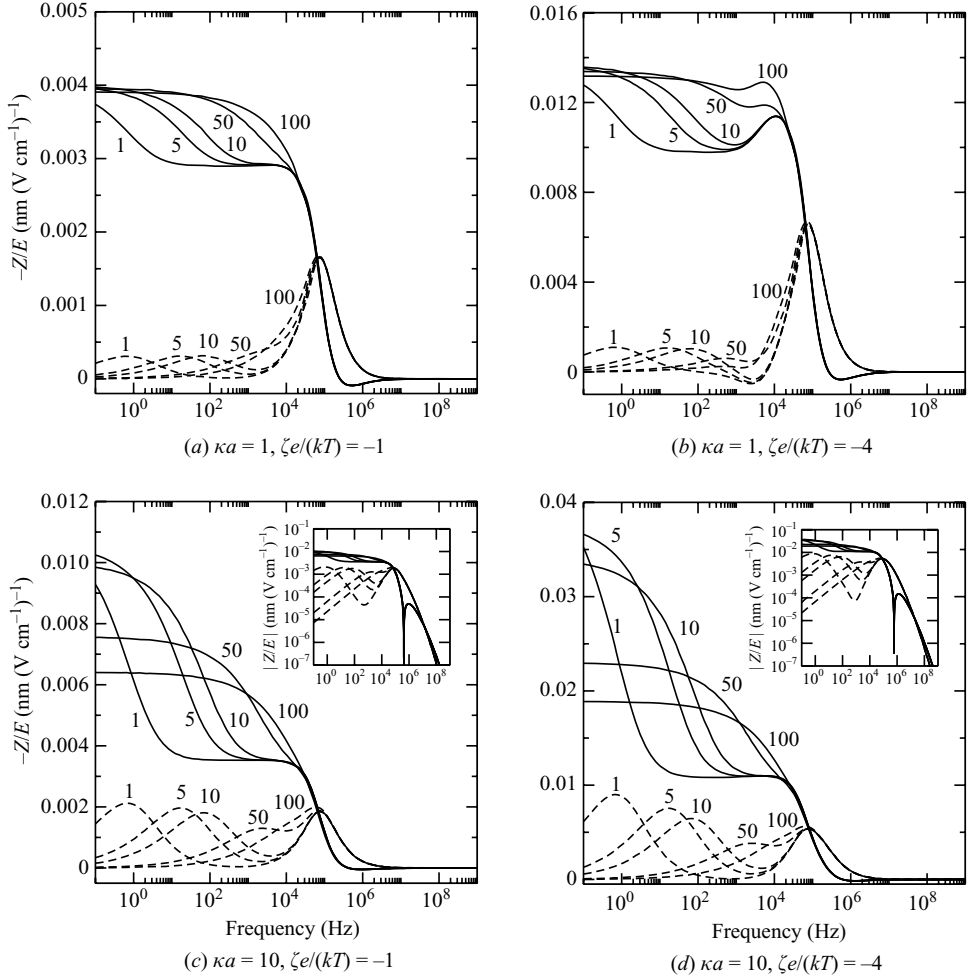
FIGURE 7. Frequency spectra of Z/E for various Brinkman screening lengths $\ell = 1, 5, 10, 50$ and $100\,\mathrm{nm}$ with scaled ζ-potentials $-\zeta e/(kT) = 1$ and 4; and scaled reciprocal double-layer thickness $\kappa a = 1$ and 10. All other parameters are the same as in figure 6. The solid and dashed lines are the real and imaginary parts of Z/E from numerical solutions of the full multi-phase electrokinetic model.

Electroacoustic signals originate from perturbations to an equilibrium base state. To linear order, these perturbations satisfy

$$\epsilon_s \epsilon_o \nabla^2 \psi' = -\rho^{e\prime}, \tag{4.1a}$$

$$-\mathrm{i}\omega n'_j = -\nabla \cdot \boldsymbol{j}_j, \tag{4.1b}$$

$$-\mathrm{i}\omega \rho_f \boldsymbol{u} = \nabla \cdot \boldsymbol{T}^f - \rho^{e\prime}\nabla\psi^0 - \rho^{e0}\nabla\psi' - \eta\ell^{-2}(\boldsymbol{u} + \mathrm{i}\omega\boldsymbol{v}), \tag{4.1c}$$

$$0 = \nabla \cdot \boldsymbol{u}, \tag{4.1d}$$

$$0 = \nabla \cdot \boldsymbol{T}^e + \eta\ell^{-2}(\boldsymbol{u} + \mathrm{i}\omega\boldsymbol{v}), \tag{4.1e}$$

where the perturbed ion fluxes are

$$\boldsymbol{j}_j = -D_j\nabla n'_j - z_j e D_j (kT)^{-1} n'_j \nabla\psi^0 - z_j e D_j (kT)^{-1} n^0_j \nabla\psi' + n^0_j \boldsymbol{u}. \tag{4.1f}$$
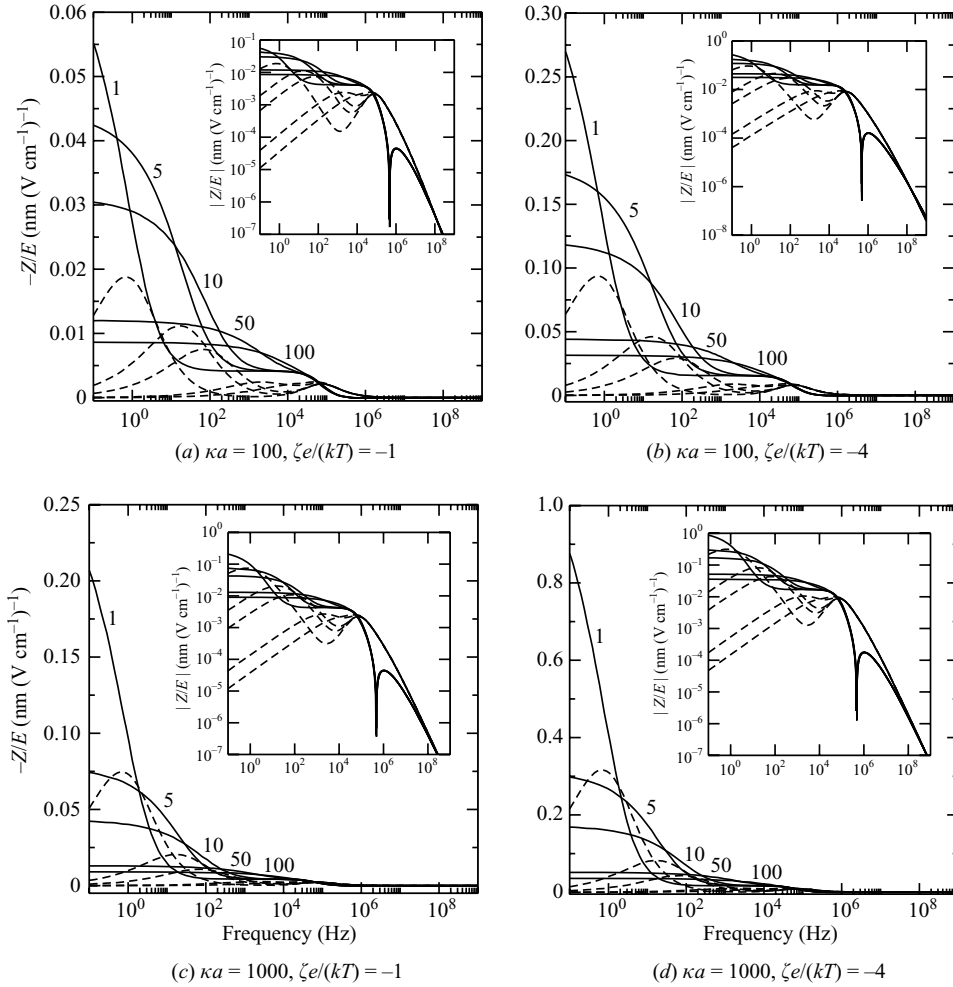
FIGURE 8. Frequency spectra of Z/E for various Brinkman screening lengths $\ell = 1, 5, 10, 50$ and 100 nm with scaled ζ-potentials $-\zeta e/(kT) = 1$ and 4; and scaled reciprocal double-layer thickness $\kappa a = 100$ and 1000. All other parameters are the same as in figure 6. The solid and dashed lines are the real and imaginary parts of Z/E from numerical solutions of the full multi-phase electrokinetic model.

Primes denote perturbed quantities, and the superscript '0' denotes the equilibrium base state. The local current density in a harmonically oscillating external field is (DeLacey & White 1981; O'Brien 1986, 1988)

$$\boldsymbol{i} = \sum_{j=1}^{N} \boldsymbol{j}_j z_j e + \mathrm{i}\omega\epsilon_o\epsilon_s\nabla\psi' \qquad (4.2)$$

and satisfies $\nabla \cdot \boldsymbol{i} = 0$.

Following O'Brien (1988, 1990), we consider an integral over a representative volume V enclosed by a surface A,

$$V^{-1}\int_A \left[\boldsymbol{u}_1 \cdot \boldsymbol{T}_2^f - \mathrm{i}\omega\boldsymbol{v}_1 \cdot \boldsymbol{T}_2^e - \boldsymbol{i}_1\psi_2' - \sum_{j=1}^{N}\frac{kT}{n_j^0}n_{j2}'\left(\boldsymbol{j}_{j1} - n_j^0\boldsymbol{u}_1\right) \right] \cdot \hat{\boldsymbol{n}} \, \mathrm{d}A \qquad (4.3)$$

for two systems '1' and '2', where $\hat{n}$ is an outward unit normal. From the linearly perturbed equations and Gauss's divergence theorem, the integral above is

$$V^{-1} \int_{V_h} \left[2\eta \mathbf{e}_1^f : \mathbf{e}_2^f - 2\mathrm{i}\omega\mu \mathbf{e}_1^e : \mathbf{e}_2^e + \eta\ell^{-2}(\mathbf{u}_1 + \mathrm{i}\omega\mathbf{v}_1) \cdot (\mathbf{u}_2 + \mathrm{i}\omega\mathbf{v}_2) \right.$$

$$\left. + \sum_{j=1}^{N} \frac{kT}{D_j n_j^0} (\mathbf{j}_{j1} - n_j^0\mathbf{u}_1) \cdot (\mathbf{j}_{j2} - n_j^0\mathbf{u}_2) \right] \mathrm{d}V$$

$$- \mathrm{i}\omega V^{-1} \int_{V_h} \left[\lambda(\nabla \cdot \mathbf{v}_1)(\nabla \cdot \mathbf{v}_2) + \rho_f \mathbf{u}_1 \cdot \mathbf{u}_2 + \epsilon_o\epsilon_s(\nabla\psi_1')\cdot(\nabla\psi_2') + \sum_{j=1}^{N} \frac{kT}{n_j^0} n_{j1}' n_{j2}' \right] \mathrm{d}V$$

$$+ V^{-1} \sum_p \int_{A_p} \left[\mathbf{u}_1 \cdot \mathbf{T}_2^f - \mathrm{i}\omega\mathbf{v}_1 \cdot \mathbf{T}_2^e - \mathbf{i}_1\psi_2' - \sum_{j=1}^{N} \frac{kT}{n_j^0} n_{j2}'(\mathbf{j}_{j1} - n_j^0\mathbf{u}_1) \right] \cdot \hat{n} \, \mathrm{d}A, \quad (4.4)$$

where $\mathbf{e}^f = (1/2)[\nabla\mathbf{u} + (\nabla\mathbf{u})^T]$ and $\mathbf{e}^e = (1/2)[\nabla\mathbf{v} + (\nabla\mathbf{v})^T]$. Note that $\sum_p$ indicates a sum over all the particles enclosed by A; A_p is the particle surface within and intersecting A; and V_h is the hydrogel volume excluding particles enclosed by A. According to O'Brien (1990), exchanging indices '1' and '2' in (4.4) does not change the integral.

If the surface A is large enough to contain many particles, and its radius of curvature is everywhere greater than the length scales associated with fluctuations of the perturbed quantities, it is a 'macroscopic boundary' and can be divided into portions that are small enough to neglect their curvature but large enough to average the perturbed quantities (O'Brien 1979). Also, for an incompressible fluid, we need to ensure that the size of A is smaller than the sound wavelength (O'Brien 1988). With these constraints, and an assumption of statistical homogeneity, (4.3) is

$$\langle \mathbf{u} \rangle_1 \cdot \nabla\langle p \rangle_2 + \langle \mathbf{i} \rangle_1 \cdot \langle \mathbf{E} \rangle_2, \quad (4.5)$$

where the angle brackets denote volume averages,

$$\langle \cdot \rangle \equiv V^{-1} \int_V (\cdot) \, \mathrm{d}V. \quad (4.6)$$

Only terms that grow with r contribute to the integral in (4.3) over the macroscopic surface A, and consequently the second and fourth terms in (4.3) are negligibly small. Surprisingly, although the polymer displacement $\mathbf{v}$ and elastic stress tensor $\mathbf{T}^e$ enter the integral in (4.3), they do not contribute to (4.5).

Since disturbances to the hydrogel–colloid composite can only be introduced through external electric fields and sound waves (pressure gradients), the electroacoustic constitutive relations are the same as for colloidal dispersions, i.e.

$$\langle \mathbf{U} \rangle = \alpha\nabla\langle p \rangle + \mu_d\langle \mathbf{E} \rangle \quad \text{and} \quad \langle \mathbf{i} \rangle = \gamma\nabla\langle p \rangle + K^*\langle \mathbf{E} \rangle, \quad (4.7)$$

where α, μ_d, γ and K^* are composite transport properties: K^* is the complex conductivity and μ_d is the particle dynamic electrophoretic mobility. Note that $\langle \mathbf{U} \rangle$ is the particle velocity averaged over all particles in V (O'Brien *et al.* 2003); it is connected to the average fluid velocity $\langle \mathbf{u} \rangle$ via the mass-averaged momentum

$$\langle \rho_0 \rangle \bar{\mathbf{u}} \equiv \langle \rho\mathbf{u} \rangle = \rho_f\langle \mathbf{u} \rangle + (\rho_p - \rho_f)\phi\langle \mathbf{U} \rangle, \quad (4.8)$$

where $\langle \rho_0 \rangle$ is the equilibrium composite density; ρ is the position dependent local density; and ϕ is the particle volume fraction.

Setting $\langle E \rangle_1 = \nabla \langle p \rangle_2 = 0$ for the two systems that differ only by the boundary conditions due to external fields and noting that (4.5) is independent of an exchange of indices, it follows that

$$\langle \boldsymbol{u} \rangle_2 \cdot \nabla \langle p \rangle_1 = \langle \boldsymbol{i} \rangle_1 \cdot \langle E \rangle_2. \tag{4.9}$$

Therefore, from the macroscopic momentum conservation equation (O'Brien 1990, §3), $\bar{\boldsymbol{u}} = 0$ if $\nabla \langle p \rangle = 0$, and together with (4.7)–(4.9) we have

$$\gamma = \rho_f^{-1}(\rho_p - \rho_f)\phi \mu_d. \tag{4.10}$$

This is the same as O'Brien's formula for colloidal dispersions (O'Brien 1990, §5), so his subsequent analysis for particulate suspensions is applicable to hydrogel–colloid composites. Accordingly, the elasticity introduced by the polymer skeleton only affects the electroacoustic response through the dynamic electrophoretic mobility

$$\mu_d = -\mathrm{i}\omega Z/E, \tag{4.11}$$

with all other macroscopic relations the same as for Newtonian colloidal dispersions.

One concern with electroacoustic characterization of hydrogel–colloid composites is whether the pressure fluctuations in an ESA experiment are measurable. In the next sections we therefore compare the dynamic electrophoretic mobilities of particles in hydrogels and Newtonian fluids at the operating frequencies of commercial electroacoustic instruments. Noteworthy is that the mobility for hydrogel composites has a comparable amplitude to those of Newtonian dispersions, but with characteristics that are sensitive to the shear modulus of the polymer skeleton. Moreover, in the relevant frequency range, the response for particles with $\kappa a \gg 1$ can be captured with the following analytical solution of the electrokinetic model.

4.2. High-frequency boundary-layer approximation

In this section we derive an approximate expression for the frequency dependent response Z/E when $\kappa a \gg 1$. The dynamics of the diffuse double layer are calculated using the surface conduction model of O'Brien (1986), which is valid when $\omega \gg a^{-2}D$. With $a \sim 1\,\mu\mathrm{m}$ and $D \sim 10^{-9}\,\mathrm{m}^2\,\mathrm{s}^{-1}$, the model is valid at frequencies above the kilohertz range in which colloidal dynamics are accessed as dynamic electrophoretic mobilities in electroacoustic experiments. We solve this problem using the decomposition and superposition methodology in §3. Briefly, the approximate asymptotic coefficients for the E and Y sub-problems are calculated, and the response Z/E is obtained by the superposition leading to (3.28). For the Y sub-problem with $\kappa a \gg 1$, we neglect the influence of surface charge, so the full model reduces to the two-fluid model addressed in §2. In this case, $C^Y = A_1$, where A_1 is given in (2.15a). For the E sub-problem, we calculate the polymer displacement and fluid velocity inside the thin double layer and match the inner and outer solutions to obtain C^E.

In our earlier publication (Wang & Hill 2008), we derived a boundary-layer approximation for the steady response Z/E given in (1.1). The contribution that depends on the particle size, and permeability and compressibility of the hydrogel, arises from terms in the inner solution that are $O[(\kappa a)^{-1}]$ smaller than the leading-order terms as $\kappa a \to \infty$. Note that hydrogel compressibility is important only if $\omega \lesssim \tau_d^{-1}$. Moreover, hydrogel–colloid composites with $a \sim 1\,\mu\mathrm{m}$, $\ell \sim 10\,\mathrm{nm}$, $\mathscr{E} \sim 1\,\mathrm{kPa}$ and $\nu \sim 0.2$ have a reciprocal draining time $\tau_d^{-1} \sim 1\,\mathrm{kHz}$ that is comparable to the lower-frequency limit of O'Brien's surface conduction model. Therefore, under conditions at which the surface conduction model is valid, the hydrogel can also be considered incompressible. Accordingly, with $\omega \gtrsim \tau_d^{-1}$ it is reasonable to neglect

the $O[(\kappa a)^{-1}]$ terms in the inner solution. This tremendously simplifies the resulting expression for Z/E.

As shown by O'Brien (1988), perturbations to the equilibrium ion concentrations in the inner and outer regions are negligible at the frequencies of interest for electroacoustics, so they do not enter the fluid momentum equation. Therefore, the perturbed electrostatic potential ψ' satisfies Laplace's equation outside the equilibrium diffuse double layer. Accordingly, in the outer region

$$\psi' = -rE\cos\theta - a^3 Pr^{-2}E\cos\theta, \qquad (4.12)$$

where P is the dipole strength. Analysis of conduction within a thin surface layer (O'Konski 1960) gives

$$P = \frac{(1-\mathrm{i}\omega') - (2Du - \mathrm{i}\omega'\epsilon_p/\epsilon_s)}{2(1-\mathrm{i}\omega') + (2Du - \mathrm{i}\omega'\epsilon_p/\epsilon_s)}, \qquad (4.13)$$

where $\omega' = \omega\epsilon_s\epsilon_o/\sigma^\infty$; $\sigma^\infty = \sum_{j=1}^{N} z_j^2 n_j^\infty D_j e^2/(kT)$ is the bulk conductivity; and $Du = \sigma^s/(\sigma^\infty a)$ is the Dukhin number (Lyklema 1995). The connection between the surface conductivity σ^s and the ζ-potential is addressed below (Lyklema 1995; Hunter 2001).

Adopting standard boundary-layer scaling (Pozrikidis 1996), the fluid and polymer momentum conservation equations (radial and tangential directions) in the inner region in which $\kappa(r-a) \ll 1$ are

$$-p_{,r} - \rho^{e0}\psi'_{,r} = 0, \qquad (4.14a)$$

$$-a^{-1}p_{,\theta} + \eta u_{\theta,rr} - \rho^{e0}a^{-1}\psi'_{,\theta} - \eta\ell^{-2}(u_\theta + \mathrm{i}\omega v_\theta) = 0, \qquad (4.14b)$$

$$(2\mu+\lambda)v_{r,rr} + (\mu+\lambda)(a\sin\theta)^{-1}(v_\theta\sin\theta)_{,r\theta} + \eta\ell^{-2}(u_r + \mathrm{i}\omega v_r) = 0, \quad (4.14c)$$

$$\mu v_{\theta,rr} + \eta\ell^{-2}(u_\theta + \mathrm{i}\omega v_\theta) = 0, \qquad (4.14d)$$

with fluid continuity equation

$$u_{r,r} + (a\sin\theta)^{-1}(u_\theta\sin\theta)_{,\theta} = 0. \qquad (4.14e)$$

Note that the equilibrium charge density $\rho^{e0} = -\kappa^2\epsilon_s\epsilon_o\zeta\exp[-\kappa(r-a)]$ when $|\zeta| \ll kT/e$ and $\kappa a \gg 1$ (Hunter 2001), and fluid inertia has been neglected inside the double layer, since it is important only beyond the gigahertz range (Hill *et al.* 2003b). For simplicity, we addresses the inner problem when $|\zeta| \ll kT/e$ before considering higher ζ-potentials.

Since p and ψ' both vary on the length scale of the particle size a, to leading order they are radially invariant in the inner region. Therefore, (4.14a) gives $p = \hat{p}E\cos\theta$, where $\hat{p}$ is a constant. By setting $u_\theta = \hat{u}_\theta(y)E\sin\theta$ and $v_\theta = \hat{v}_\theta(y)E\sin\theta$, where $y = r - a$, the tangential equations (4.14b) and (4.14d) become

$$\eta\hat{u}_{\theta,yy} - \eta\ell^{-2}(\hat{u}_\theta + \mathrm{i}\omega\hat{v}_\theta) = -a^{-1}\hat{p} - \zeta\kappa^2\epsilon_s\epsilon_o(1+P)\exp(-\kappa y), \qquad (4.15)$$

$$\mu\hat{v}_{\theta,yy} + \eta\ell^{-2}(\hat{u}_\theta + \mathrm{i}\omega\hat{v}_\theta) = 0. \qquad (4.16)$$

With boundary conditions $\hat{v}_\theta = \hat{u}_\theta = 0$ at $y = 0$ and finite $\hat{v}_\theta$ and $\hat{u}_\theta$ as $y \to \infty$, the solutions are

$$\hat{u}_\theta = i\omega\epsilon_s\epsilon_o\zeta(1 + P)(\mu - i\omega\eta)^{-1}[\exp(-\kappa y) - 1] - \mu c_1\eta^{-1}\exp(-sy)$$
$$+ \hat{p}\mu[\eta a(\mu - i\omega\eta)s^2]^{-1} + \mu\kappa^2\epsilon_o\epsilon_s\zeta(1 + P)[\eta(\mu - i\omega\eta)(s^2 - \kappa^2)]^{-1}\exp(-\kappa y), \quad (4.17)$$

$$\hat{v}_\theta = -\epsilon_s\epsilon_o\zeta(1 + P)(\mu - i\omega\eta)^{-1}[\exp(-\kappa y) - 1] + c_1\exp(-sy) - \hat{p}[a(\mu - i\omega\eta)s^2]^{-1}$$
$$- \kappa^2\epsilon_o\epsilon_s\zeta(1 + P)[(\mu - i\omega\eta)(s^2 - \kappa^2)]^{-1}\exp(-\kappa y), \quad (4.18)$$

where $s^2 = (\mu - i\omega\eta)(\mu\ell^2)^{-1}$ with $\mathrm{Re}(s) > 0$. The no-slip boundary conditions at $y = 0$ require

$$c_1 = \hat{p}[(\mu - i\omega\eta)s^2 a]^{-1} + \kappa^2\epsilon_s\epsilon_o\zeta(1 + P)[(\mu - i\omega\eta)(s^2 - \kappa^2)]^{-1}. \quad (4.19)$$

For the inner solution to be finite as $y \to \infty$, the terms that are linear and quadratic in y must be neglected. Integrating (4.14e) gives $u_r = \hat{u}_r(y)E\cos\theta$, where

$$\hat{u}_r = -2a^{-1}\int_0^y \hat{u}_\theta(y')\,\mathrm{d}y'$$
$$= 2\epsilon_s\epsilon_o\zeta(1 + P)[\kappa a(\mu - i\omega\eta)]^{-1}\{i\omega + \mu\kappa^2[\eta(s^2 - \kappa^2)]^{-1}\}[\exp(-\kappa y) - 1]$$
$$- 2\mu c_1(\eta s a)^{-1}[\exp(-sy) - 1]. \quad (4.20)$$

Note that setting $\omega = 0$ recovers the steady solutions derived in earlier works (Hill 2006a; Wang & Hill 2008).

Finally, integrating (4.14c) gives $v_r = \hat{v}_r(y)E\cos\theta$, where

$$\hat{v}_r = c_2\exp(-ny) - a_1(n^2 - \kappa^2)^{-1}\exp(-\kappa y) - a_2(n^2 - s^2)^{-1}\exp(-sy)$$
$$+ a_3[n^{-2} - (n^2 - \kappa^2)\exp(-\kappa y)] + a_4[n^{-2} - (n^2 - s^2)\exp(-sy)] \quad (4.21)$$

with $n^2 = -i\omega\eta[\ell^2(2\mu + \lambda)]^{-1}$ and $\mathrm{Re}(n) > 0$,

$$a_1 = -(\mu + \lambda)\kappa\epsilon_s\epsilon_o\zeta(1 + P)[a(2\mu + \lambda)(\mu - i\omega\eta)]^{-1}[1 + \kappa^2(s^2 - \kappa^2)^{-1}], \quad (4.22a)$$
$$a_2 = (\mu + \lambda)sc_1[a(2\mu + \lambda)]^{-1}, \quad (4.22b)$$
$$a_3 = -\eta\epsilon_s\epsilon_o\zeta(1 + P)[\kappa a\ell^2(2\mu + \lambda)(\mu - i\omega\eta)]^{-1}\{i\omega + \mu\kappa^2[\eta(s^2 - \kappa^2)]^{-1}\}, \quad (4.22c)$$
$$a_4 = \mu c_1[\ell^2 sa(2\mu + \lambda)]^{-1}, \quad (4.22d)$$

and c_2 is chosen to ensure $\hat{v}_r = 0$ at $y = 0$.

In the outer region, the governing equations are the same as the two-fluid model in §2, giving

$$\boldsymbol{u} = A_1^E\nabla(r^{-2}\boldsymbol{E}\cdot\boldsymbol{e}_r) + \sum_{j=1}^{2}B_j^E\nabla \times [h(K_j r)\boldsymbol{E} \times \boldsymbol{e}_r], \quad (4.23a)$$

$$\boldsymbol{v} = mA_1^E\nabla(r^{-2}\boldsymbol{E}\cdot\boldsymbol{e}_r) + A_2^E\nabla[h(kr)\boldsymbol{E}\cdot\boldsymbol{e}_r] + \sum_{j=1}^{2}M_j B_j^E\nabla \times [h(K_j r)\boldsymbol{E} \times \boldsymbol{e}_r], \quad (4.23b)$$

where k, m, K_j and M_j ($j = 1, 2$) are also the same as in §2. Note that the asymptotic coefficient $C^E = A_1^E$ is determined by matching the inner and outer solutions.

From (2.2a), the pressure in the outer region is

$$p = i\omega\rho_f A_1^E r^{-2}E\cos\theta - i\omega\eta\ell^{-2}A_2^E h(kr)E\cos\theta, \quad (4.24)$$

so

$$\hat{p} = i\omega\rho_f A_1^E a^{-2} - i\omega\eta\ell^{-2} A_2^E h(ka). \tag{4.25}$$

Matching the inner solutions as $y \to \infty$,

$$u_\theta = -i\omega(\mu - i\omega\eta)^{-1}\epsilon_s\epsilon_o\zeta(1 + P)E\sin\theta \text{ and } u_r = 0, \tag{4.26a}$$

$$v_\theta = (\mu - i\omega\eta)^{-1}\epsilon_s\epsilon_o\zeta(1 + P)E\sin\theta \text{ and } v_r = 0, \tag{4.26b}$$

to the outer solutions (4.23a) and (4.23b) as $r \to a$ gives

$$A_1^E = a^3\epsilon_s\epsilon_o\zeta(1 + P)(-i\omega\eta\mu^{-1}\Theta^E + \Gamma^E)[(\mu - i\omega\eta)H]^{-1}, \tag{4.27a}$$

where, from b and β_j ($j = 1,2$) in §2,

$$\Theta^E = -\mu\eta^{-1}\{ib^2(M_1 - M_2)(\beta_1 + i)(\beta_2 + i)$$
$$+ (b^2 + 2ib - 2)[M_1\beta_1^2(\beta_2 + i) - M_2\beta_2^2(\beta_1 + i)]\}, \tag{4.27b}$$

$$\Gamma^E = (b^2 + 2ib - 2)[\beta_1^2(\beta_2 + i) - \beta_2^2(\beta_1 + i)]. \tag{4.27c}$$

Note that the matching is achieved by neglecting asymptotically small terms as $\kappa a \to \infty$ and $\ell/a \to 0$.

Next, we establish the connection between the Dukhin number Du and ζ-potential for hydrogels to determine P. This relation is not the same as for Newtonian electrolytes because the polymer skeleton modulates the convective transport of ions (O'Brien 1986). Following a similar procedure for obtaining (4.17), the tangential velocity in the double layer as $\kappa a \to \infty$ is

$$u_\theta = i\omega\epsilon_s\epsilon_o(\mu - i\omega\eta)^{-1}(\psi^0 - \zeta)\nabla_s\psi', \tag{4.28}$$

where ∇_s is the tangential gradient operator.

Although (4.28) is derived for $|\zeta| \ll kT/e$, the vanishing of the equilibrium electrostatic potential ψ^0 outside the double layer permits (4.28) to be generalized for any ζ-potential. Therefore, using (4.28) and the definition of Du and σ^s (O'Brien 1986; Lyklema 1995), for symmetrical z–z electrolytes with $|\zeta| \ll kT/e$, we find

$$Du = (z^2 + 3m)(2\kappa a)^{-1}[\zeta e/(kT)]^2, \tag{4.29}$$

where $m = -2i\omega\epsilon_s\epsilon_o[3D(\mu - i\omega\eta)]^{-1}(kT/e)^2$ and $D = D_1 = D_2$ is the ion diffusivity. For general electrolytes and higher ζ-potentials (O'Brien 1986), we find

$$Du = \frac{n_i^\infty z_i^2 D_i\sqrt{2}}{\sum_{j=1}^N z_j^2 n_j^\infty D_j}\left(1 + \frac{3m_i}{z_i^2}\right)\frac{\exp[-ez_i\zeta/(2kT)]}{\kappa_i a} \tag{4.30}$$

when $\exp[-ez_i\zeta/(2kT)] \gg 1$. Here, the subscript 'i' refers to the counterion with highest charge and

$$m_i = -2i\omega\epsilon_s\epsilon_o[3D_i(\mu - i\omega\eta)]^{-1}(kT/e)^2, \tag{4.31}$$

$$\kappa_i^2 = (z_i^2 e^2 n_i^\infty)(\epsilon_s\epsilon_o kT)^{-1}. \tag{4.32}$$

Finally, superposing the Y and E sub-problems and accounting for fluid and particle inertia (Appendix D), the dynamic electric-field-induced response is

$$Z/E = \epsilon_s\epsilon_o\zeta(1 + P)(\mu - i\omega\eta)^{-1}G, \tag{4.33}$$

where

$$G = \frac{-i\omega\eta\mu^{-1}\Theta^E + \Gamma^E}{(\Theta + \Gamma)/2 - i\omega H(\rho_p - \rho_f)/(3\rho_f)}. \tag{4.34}$$
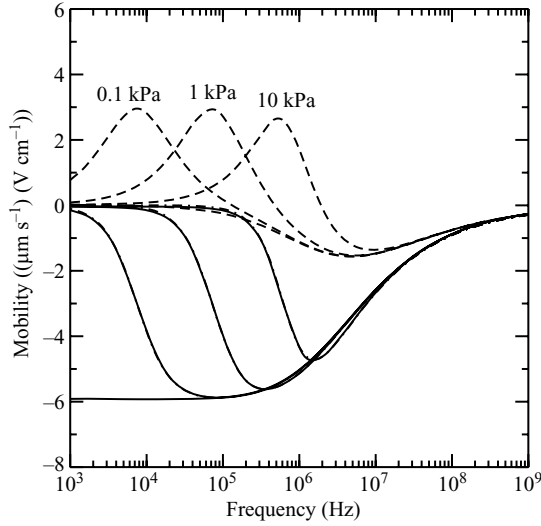
FIGURE 9. Frequency spectra of the dynamic electrophoretic mobility $\mu_d = -i\omega Z/E$ for Young's moduli $\mathscr{E} = 0.1$, 1 and 10 kPa with Poisson's ratio $\nu = 0.2$. Other parameters are the same as in figure 2. The solid and dashed lines are the real and imaginary parts of μ_d from numerical solutions of the full multi-phase electrokinetic model. The dash-dotted lines (barely visible because they overlap numerical solutions) are the real parts of μ_d from the analytical approximation (4.33); the imaginary parts of μ_d from (4.33) are not shown because they overlap the numerical solutions. Note that the spectrum with a finite (real) low-frequency plateau is the mobility $\mu_d^* = -i\omega(Z/E)^*$ for the same particles dispersed in a Newtonian electrolyte without polymer (Hill *et al.* 2003*a*).

Recall that this approximation is valid for frequencies $\omega/(2\pi) \gg a^{-2}D$, $\omega/(2\pi) \gg \tau_d^{-1}$ and $\omega/(2\pi) \ll \kappa^2 \eta \rho_f^{-1}$ with $\kappa a \gg 1$. Noteworthy is that (4.33) produces the same mobility as O'Brien's formula (3.31) evaluated with a complex shear viscosity $\eta^* = \eta + i\mu\omega^{-1}$. Thus, while our independent analysis made no assumptions concerning hydrogel compressibility and hydrodynamic permeability in the inner region, where electro-osmotic flow is active, the dynamics at frequencies above the reciprocal draining time τ_d^{-1} are found to occur with negligible relative motion of the fluid and polymer phases.

4.3. *Comparison of numerical and analytical approximate solutions*

The amplitude of the dynamic electrokinetic response Z/E was demonstrated in § 3.4 to become vanishingly small at high frequencies. The results below demonstrate that Z/E decays with frequency in a manner in which the dynamic mobility $\mu_d = -i\omega Z/E$ is finite at the frequencies used in commercial electroacoustic instruments. In § 4.1 we showed that O'Brien's macroscopic electroacoustic equations (O'Brien 1990) can be applied to hydrogel–colloid composites. Accordingly, a close connection was established between the electroacoustic signal (pressure fluctuations) in ESA measurements and the dynamic mobility. This motivated the derivation in § 4.2, leading to the analytical approximation (4.33) for the high frequencies encountered in electroacoustic experiments.

The dynamic electrophoretic mobilities for representative hydrogel–colloid composites from (4.33) and numerical computations are presented in figure 9. Because our calculations of the dynamic mobility neglect interactions, the results are suitable for composites with low particle volume fractions. Spectra are shown

with Young's modulus spanning three decades. Note that the spectrum with a finite plateau (real part) at low frequencies is the mobility for the same particles dispersed in a Newtonian electrolyte without polymer; this was calculated using the MPEK software package (Hill *et al.* 2003a). At this large value of $\kappa a = 500$, the analytical approximation (4.33) compares extremely well with the numerical calculations. Note also that the real parts (dash-dotted and solid lines) depart very slightly when the amplitude vanishes at lower frequencies, and the imaginary parts are practically identical at all frequencies.

Noteworthy is that the real part of μ_d can be distinguished from μ_d^* only at megahertz frequencies when Young's modulus of the skeleton is greater than about 10 kPa. However, the imaginary part is very sensitive to the elastic modulus at about 1 MHz, suggesting that at a given fixed frequency, or in a narrow range of frequencies, an electroacoustic experiment could probe the kinetics of polymer gelation and aging. Recall that commercial electroacoustic instruments operate at frequencies between 0.3 MHz and 11 MHz (Hunter 1998). Clearly, to probe the elastic modulus of hydrogel skeletons with lower moduli, a wider frequency range – extending to lower frequencies – is required. Nevertheless, many important hydrogels have an elastic modulus greater than 10 kPa; e.g. reverse thermoresponsive poly(N-isopropylacrylamide) gels at 8 wt% and 40°C have $\mathscr{E} \approx 170$ kPa (Takigawa *et al.* 1997), and polyacrylamide gels at 0.8 % w/v have $\mathscr{E} \approx 35$ kPa (Takigawa *et al.* 1996), so the real and imaginary parts of their electroacoustic response at megahertz frequencies would be particularly sensitive to changes in the elastic modulus. Note also that because the electroacoustic response is prominent at frequencies much higher than the reciprocal draining time, the response only reflects changes in the shear modulus, not the accompanying changes in hydrodynamic permeability.

Figure 10 compares numerical calculations of the dynamic electrophoretic mobility with our analytical boundary-layer approximation (4.33) with $\kappa a = 50$ (top panels) and $\kappa a = 1000$ (bottom panels). This approximation is accurate when $\kappa a = 1000$ for all the experimentally accessible ζ-potentials and frequencies, and even when $\kappa a = 50$ the approximation deviates only slightly from the exact calculations at the highest ζ-potentials and frequencies. Thus, as expected, our analytical solution is demonstrated to be valid for small Dukhin numbers Du. The foregoing dynamics are independent of the Brinkman screening length and Poisson ratio (with fixed shear modulus), as is clearly evident when applying O'Brien's dynamic mobility formula (3.31) evaluated with a complex shear viscosity $\eta^* = \eta + \mathrm{i}\mu\omega^{-1}$. Note that (4.33) does not capture the compressible dynamics at frequencies below the reciprocal draining time (see § 3), where the dynamic mobility is vanishingly small.

5. Summary

We extended the multi-phase electrokinetic model of Hill & Ostoja-Starzewski (2008) and Wang & Hill (2008) to calculate the dynamic response of a charged, spherical colloid embedded in an uncharged hydrogel subjected to harmonically oscillating electric field. We began by solving the two-fluid model of Levine & Lubensky (2001) exactly and compared our analytical solution with approximations widely adopted in the microrheolgy literature. We then developed a computational methodology to solve the full multi-phase electrokinetic model by linearly perturbing an equilibrium base state governed by the nonlinear Poisson–Boltzmann equation.

Our exact analytical solution of the two-fluid model of Levine & Lubensky (2001) agrees well with their approximate solution when fluid and particle inertia can be
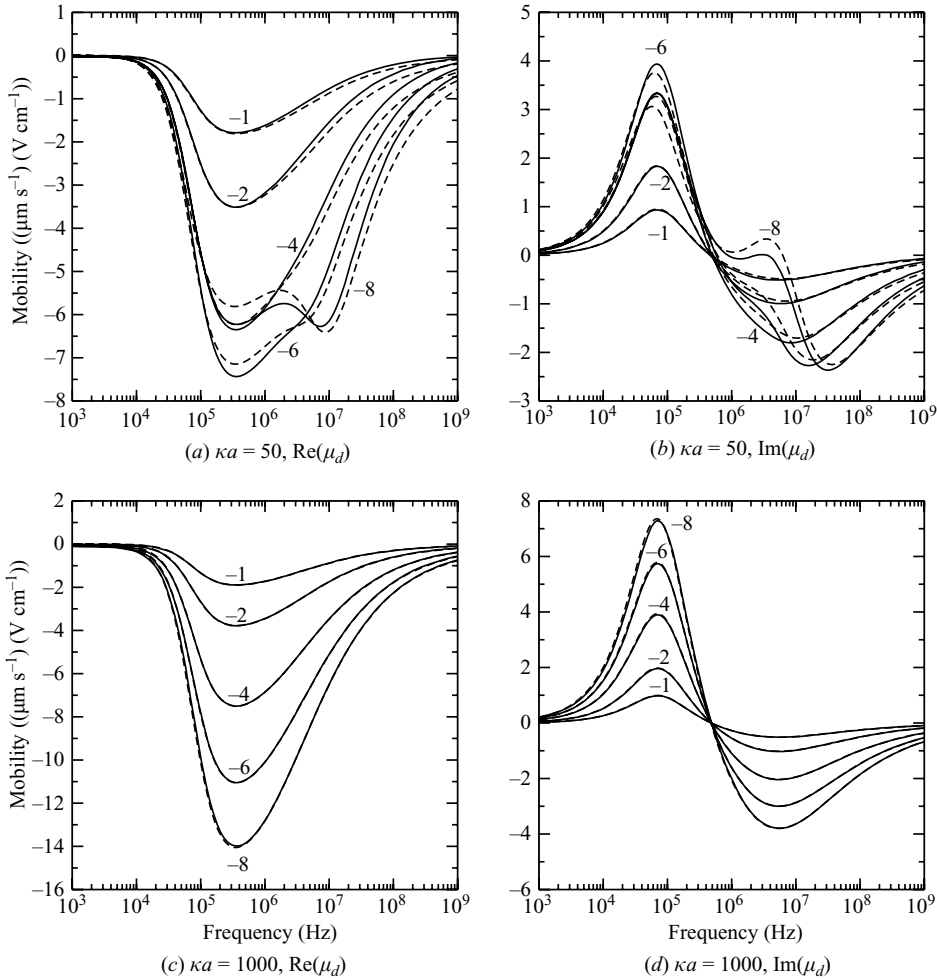
FIGURE 10. Frequency spectra of the dynamic electrophoretic mobility $\mu_d = -i\omega Z/E$ for various scaled ζ-potentials $-\zeta e/(kT) = 1$, 2, 4, 6 and 8: (*a*, *b*) $\kappa a = 50$ and (*c*, *d*) $ka = 1000$. All other parameters are the same as in figure 6. The solid lines are the (*a*, *c*) real and (*b*, *d*) imaginary parts of μ_d from numerical solutions of the full multi-phase electrokinetic model, and the dashed lines are μ_d from the analytical boundary-layer approximation (4.33).

neglected. At frequencies above the reciprocal draining time, where the skeleton dynamics are incompressible, our solution shows that inertial influences are captured by the unsteady Stokes equations with a complex shear viscosity.

The electric-field-induced particle response, defined as the ratio of the displacement to the electric field strength, was obtained by superposing two simpler sub-problems to satisfy the particle equation of motion. Compressible and incompressible hydrogel skeletons were addressed independently. By adopting an analytical solution in the far field, we achieved accurate numerical solutions over an extraordinarily wide range of frequencies, for a wide range of the experimentally accessible parameter space.

In addition, we examined the dynamic electrophoretic mobility, defined as the ratio of the particle velocity to the electric field strength, and its connection to electroacoustic diagnostics for characterizing hydrogel–colloid composites. Noteworthy was an analytical boundary-layer approximation for thin double layers

($\kappa a \gg 1$) that compares well with numerics at the ultrasonic frequencies adopted in commercial electroacoustic instruments.

The electrical response of a colloidal particle in a hydrogel often exhibits an ostensible transition from quasi-steady compressible to incompressible viscoelastic dynamics – both characterized by distinct plateaus in the real part of the frequency spectrum – as the frequency passes through the reciprocal draining time τ_d^{-1}.

At frequencies above τ_d^{-1}, the response is the same as in a Newtonian electrolyte with a complex shear viscosity. Accordingly, the dynamics are practically independent of the hydrogel permeability, since the incompressible fluid and polymer skeleton move together. At frequencies below τ_d^{-1}, however, the dynamics of compressible and incompressible hydrogels are qualitatively different. Hydrogel compressibility can increase the electric-field-induced particle displacement by an order of magnitude relative to the displacement in a perfectly incompressible skeleton with the same shear modulus. In general, the response depends on Poisson's ratio, Young's modulus and Brinkman screening length of the hydrogel, as well as physicochemical characteristics of the inclusions, including size and charge. For inclusions with thick double layers ($\kappa a \lesssim 1$) and high ζ-potentials ($\zeta \gtrsim 2kT/e$), the electrical response spectrum is influenced by polarization and relaxation of the diffuse double layer.

The present theory provides a rigorous foundation for interpreting two classes of electric-field-based diagnostic experiments involving hydrogel–colloid composites. Such experiments probe both the physicochemical characteristics of the charged inclusions and the viscoelastic rheology of the hydrogel. Our calculations demonstrate that the particle displacement at low frequencies could be directly measured using active electrical microrheology. At higher frequencies, however, the particle displacements are too small (sub-nanometre) to register with particle-tracking microscopy, so electroacoustic techniques are necessary to measure instead the dynamic electrophoretic mobility. Accordingly, we showed that the macroscopic relations for colloidal dispersions developed by O'Brien (1990) can be directly applied to hydrogel–colloid composites. Our calculations of the dynamic electrophoretic mobility demonstrate that the strength of electroacoustic signals from hydrogel–colloid composites are comparable to those from Newtonian electrolytes without a polymer skeleton. The high frequencies in such experiments guarantee incompressible skeleton dynamics, so the response is independent of skeleton permeability and intrinsic compressibility.

Finally, we note that many synthetic hydrogels and, particularly, biopolymer networks are charged, and even ideally uncharged gels (e.g. polyacrylamide) become weakly charged due to hydrolysis (e.g. Kizilay & Okay 2003). The influence of charge on the susceptibility and electrical response of inclusions in charged networks will be addressed in a forthcoming publication (Mohammadi & Hill, submitted).

Appendix A. Incompressible hydrogel skeletons

For incompressible hydrogels, the second term in (3.2e) is singular because $\lambda \to \infty$ as $\nu \to 1/2$. However, similar to Hill & Ostoja-Starzewski (2008), the displacement can

be expanded as a power series in a small parameter $\epsilon = 1 - 2\nu$, i.e. $\boldsymbol{v} = \boldsymbol{v}_0 + \epsilon\boldsymbol{v}_1 + \cdots$, which, after substituting into (3.2e) and collecting terms of like order in ϵ, gives

$$\nabla \cdot \boldsymbol{v}_0 = 0 \qquad (\text{A}\,1a)$$

at $O(\epsilon^{-1})$ and

$$\mu[\nabla^2\boldsymbol{v}_0 + \nabla(\nabla\cdot\boldsymbol{v}_1)] + \eta\ell^{-2}(\boldsymbol{u} + \mathrm{i}\omega\boldsymbol{v}_0) = 0 \qquad (\text{A}\,1b)$$

at $O(1)$. Note that $-\mu\nabla\cdot\boldsymbol{v}_1$ in (A 1b) can be replaced by a pressure, so (A 1a) and (A 1b) are equivalent to the unsteady Stokes equations with a body force $\eta\ell^{-2}(\boldsymbol{u}+\mathrm{i}\omega\boldsymbol{v}_0)$.

Since $\nabla\cdot\boldsymbol{v}_0 = 0$, the leading-order displacement may be constructed as

$$\boldsymbol{v}_0 = \nabla\times\nabla\times[g(r)\boldsymbol{X}] + \boldsymbol{Y}. \qquad (\text{A}\,2)$$

Taking the curl of (A 1b) and (3.2c), the fluid momentum and incompressible polymer elasticity equations become

$$-\mathrm{i}\omega\rho_f\mathscr{L}_1 f_{,r} = \eta\mathscr{L}_2 f_{,rrr} - \eta\ell^{-2}(\mathscr{L}_1 f_{,r} + \mathrm{i}\omega\mathscr{L}_1 g_{,r})$$
$$-\sum_{j=1}^{N} z_j er^{-1}\{\hat{n}_j\psi_{,r}^0 - n_{j,r}^0[\hat{\psi} - r(E/X)]\}, \qquad (\text{A}\,3)$$

$$0 = \mu\mathscr{L}_2 g_{,rrr} + \eta\ell^{-2}(\mathscr{L}_1 f_{,r} + \mathrm{i}\omega\mathscr{L}_1 g_{,r}) \qquad (\text{A}\,4)$$

with boundary conditions

$$g_{,r} = (a/2)(Y/X) \quad\text{and}\quad g_{,rr} = (1/2)(Y/X) \text{ at } r = a, \qquad (\text{A}\,5)$$
$$g_{,r}\to 0 \quad\text{and}\quad g_{,rr}\to 0 \text{ as } r\to\infty. \qquad (\text{A}\,6)$$

It is expedient to write (A 3) and (A 4) as

$$\mathscr{L}_2\begin{pmatrix} f_{,rrr} \\ g_{,rrr} \end{pmatrix} + \boldsymbol{M}\,\mathscr{L}_1\begin{pmatrix} f_{,r} \\ g_{,r} \end{pmatrix} = \begin{pmatrix} \eta^{-1}\sum_{j=1}^{N} z_j er^{-1}\{\hat{n}_j\psi_{,r}^0 - n_{j,r}^0[\hat{\psi} - r(E/X)]\} \\ 0 \end{pmatrix}, \quad (\text{A}\,7)$$

where

$$\boldsymbol{M} = \begin{pmatrix} \mathrm{i}\omega\rho_f\eta^{-1} - \ell^{-2} & -\mathrm{i}\omega\ell^{-2} \\ \eta\mu^{-1}\ell^{-2} & \mathrm{i}\omega\eta\mu^{-1}\ell^{-2} \end{pmatrix}. \qquad (\text{A}\,8)$$

Functions $f(r)$ and $g(r)$ are decoupled by diagonalizing $\boldsymbol{M}$ as

$$\boldsymbol{M} = \boldsymbol{R}\begin{pmatrix} \lambda_1 & 0 \\ 0 & \lambda_2 \end{pmatrix}\boldsymbol{R}^{-1}, \qquad (\text{A}\,9)$$

where λ_1 and λ_2 are the eigenvalues of $\boldsymbol{M}$, and the columns of $\boldsymbol{R}$ are the corresponding eigenvectors. Substituting $\boldsymbol{M}$ into (A 7) and introducing

$$\begin{pmatrix} h_1(r) \\ h_2(r) \end{pmatrix} \equiv \boldsymbol{R}^{-1}\begin{pmatrix} f(r) \\ g(r) \end{pmatrix} \qquad (\text{A}\,10)$$

give

$$\mathscr{L}_2\begin{pmatrix} h_{1,rrr} \\ h_{2,rrr} \end{pmatrix} + \mathscr{L}_1\begin{pmatrix} \lambda_1 h_{1,r} \\ \lambda_2 h_{2,r} \end{pmatrix} = \boldsymbol{R}^{-1}\begin{pmatrix} \eta^{-1}\sum_{j=1}^{N} z_j er^{-1}\{\hat{n}_j\psi_{,r}^0 - n_{j,r}^0[\hat{\psi} - r(E/X)]\} \\ 0 \end{pmatrix},$$
$$(\text{A}\,11)$$

which replaces (3.6), (3.8) and (3.9) in the main text for compressible hydrogels. Note that $f_{,r}$ in the perturbed ion-conservation equations (3.11) is expressed as a linear combination of h_1 and h_2 according to (A 10).

Appendix B. Far-field asymptotics for compressible hydrogel skeletons

The far-field boundary conditions in §3.2 cannot be applied directly, because more information concerning the functional forms of the solutions as $r \to \infty$ is required to avoid numerical instabilities. Beyond the equilibrium double layer, i.e. where $r \gg a + \kappa^{-1}$, the equilibrium electrostatic potential ψ^0 and ion concentrations n_j^0 decay rapidly (exponentially) to their far-field values ($\psi^0 \to 0$ and $n_j^0 \to n_j^\infty$) as $r \to \infty$, and the equations for the perturbations simplify to two decoupled sets. The first set comprises the Poisson and ion-conservation equations,

$$\epsilon_s \epsilon_o \nabla^2 \psi' + \sum_{j=1}^N z_j n_j' e = 0, \tag{B 1a}$$

$$\mathrm{i}\omega n_j' + z_j e D_j n_j^\infty (kT)^{-1} \nabla^2 \psi' + D_j \nabla^2 n_j' = 0, \tag{B 1b}$$

and the other is identical to (2.2a)–(2.2c) in §2.

In contrast with the electrokinetic model, these equations have an analytical solution. We begin by considering the first set of equations involving the perturbed potential ψ'' and ion concentrations n_j' and then establish the connection between the asymptotic forms of $f_{,r}$, g_1 and g_2 given in §3.2 and the exact solution of the two-fluid model in §2.

B.1. *Far-field decays of $\hat{\psi}$ and $\hat{n}_j$*

Equations (B 1a) and (B 1b) can be written as

$$\epsilon_s \epsilon_o \mathscr{L}_1 \hat{\psi} + \sum_{j=1}^N z_j \hat{n}_j e = 0, \tag{B 2a}$$

$$D_j \mathscr{L}_1 \hat{n}_j - z_j e^2 D_j n_j^\infty (\epsilon_s \epsilon_o kT)^{-1} \sum_{k=1}^N z_k \hat{n}_k + \mathrm{i}\omega \hat{n}_j = 0, \tag{B 2b}$$

or

$$\mathscr{L}_1 \begin{pmatrix} \hat{n}_1 \\ \hat{n}_2 \\ \vdots \\ \hat{n}_N \\ \hat{\psi} \end{pmatrix} + \boldsymbol{P} \begin{pmatrix} \hat{n}_1 \\ \hat{n}_2 \\ \vdots \\ \hat{n}_N \\ \hat{\psi} \end{pmatrix} = 0, \tag{B 3}$$

where

$$\boldsymbol{P} = \frac{e^2}{\epsilon_s \epsilon_o kT} \begin{pmatrix} \frac{\mathrm{i}\omega\epsilon_s\epsilon_o kT}{e^2 D_1} - n_1^\infty z_1^2 & -n_1^\infty z_1 z_2 & \cdots & -z_1 n_1^\infty z_2 - n_1^\infty z_1 z_N & 0 \\ -n_2^\infty z_2 z_1 & \frac{\mathrm{i}\omega\epsilon_s\epsilon_o kT}{e^2 D_2} - n_2^\infty z_2^2 & \cdots & -n_2^\infty z_2 z_N & 0 \\ \vdots & \vdots & \ddots & \vdots & \vdots \\ -n_N^\infty z_N z_1 & -n_N^\infty z_N z_2 & \cdots & \frac{\mathrm{i}\omega\epsilon_s\epsilon_o kT}{e^2 D_N} - n_N^\infty z_N^2 & 0 \\ z_1 kT/e & z_2 kT/e & \cdots & z_N kT/e & 0 \end{pmatrix}. \tag{B 4}$$

Similar to the incompressible problem, matrix $\boldsymbol{P}$ can be diagonalized as

$$\boldsymbol{P} = \boldsymbol{Q} \begin{pmatrix} \gamma_1 & 0 & \cdots & 0 \\ 0 & \gamma_2 & \cdots & 0 \\ \vdots & \vdots & \ddots & \vdots \\ 0 & 0 & \cdots & \gamma_{N+1} \end{pmatrix} \boldsymbol{Q}^{-1}, \tag{B 5}$$

where γ_k ($k = 1, 2, \ldots, N+1$) are the eigenvalues of $\boldsymbol{P}$, and the kth column of $\boldsymbol{Q}$ is the corresponding eigenvector. By setting

$$\begin{pmatrix} \chi_1 \\ \chi_2 \\ \vdots \\ \chi_N \\ \chi_{N+1} \end{pmatrix} \equiv \boldsymbol{Q}^{-1} \begin{pmatrix} \hat{n}_1 \\ \hat{n}_2 \\ \vdots \\ \hat{n}_N \\ \hat{\psi} \end{pmatrix}, \tag{B 6}$$

we obtain a set of simpler equations

$$\mathscr{L}_1 \chi_k + \gamma_k \chi_k = 0 \quad (k = 1, 2, \ldots, N+1), \tag{B 7}$$

where $\chi_k = \chi_k(r)$. Using standard techniques (Lamb 1945; Oestreicher 1951; MacRobert 1967; Temkin & Leung 1976; Markov 2005), the solutions of (B 7) are

$$\chi_k(r) = D_k h(\sqrt{\gamma_k} r) \text{ when } \gamma_k \neq 0, \tag{B 8a}$$
$$\chi_k(r) = D_k r^{-2} \text{ when } \gamma_k = 0, \tag{B 8b}$$

where D_k are unknown constants. From (B 4), $\boldsymbol{P}$ has only one $\gamma_k = 0$, and to ensure decaying solutions as $r \to \infty$, $\mathrm{Im}(\sqrt{\gamma_k}) > 0$ for all $\gamma_k \neq 0$.

Equation (B 7) demonstrates that χ_k are decoupled in the far field. Therefore $\hat{n}_j$ and $\hat{\psi}$ can be constructed by inverting (B 6). Dividing the far-field expressions for χ_k by their first derivative eliminates the constants D_k, and therefore the boundary conditions for χ_k as $r \to \infty$ are

$$\chi_k - [h(\sqrt{\gamma_k} r)/h'(\sqrt{\gamma_k} r)]\chi_{k,r} = 0 \text{ at } r = r_{max} \text{ when } \gamma_k \neq 0, \tag{B 9}$$
$$\chi_k + (r/2)\chi_{k,r} = 0 \text{ at } r = r_{max} \text{ when } \gamma_k = 0, \tag{B 10}$$

where r_{max} is the maximum radial extent of the numerical calculations in which $a \leqslant r \leqslant r_{max}$. Note that the kth column of $\boldsymbol{Q}$ corresponding to $\gamma_k = 0$ has only one non-zero entry, which equals one, and the dipole strength of the electrostatic potential is

$$D^X = r_{max}^2 \chi_k(r_{max}) \text{ when } \gamma_k = 0 \text{ as } r_{max} \to \infty. \tag{B 11}$$

B.2. *Far-field decays of $f_{,r}$, g_1 and g_2*

Since the electrical body force vanishes far from the particle, i.e. where $r \gg a + \kappa^{-1}$, the fluid velocity and polymer displacement in §2 can be used to construct $f_{,r}(r)$, $g_1(r)$ and $g_2(r)$ in the far field. These provide boundary conditions at $r = r_{max}$ for the numerical solution in the region in which $a \leqslant r \leqslant r_{max}$ with $r_{max} \gg a + \kappa^{-1}$.

From §3.2, the radial and tangential components of the fluid velocity are

$$u_r = [-2r^{-1} f_{,r} - i\omega(Y/X)]X \cos\theta, \tag{B 12a}$$
$$u_\theta = [-r^{-1} f_{,r} - f_{,rr} - i\omega(Y/X)](-X \sin\theta), \tag{B 12b}$$

and the radial and tangential components of the polymer displacement are

$$v_r = [g_1 + g_2 - (Y/X)]X\cos\theta, \tag{B 12c}$$

$$v_\theta = [g_1 - (Y/X)](-X\sin\theta). \tag{B 12d}$$

Equating these to the exact solution in §2 with $X = Y$ gives

$$f_{,r}^\infty = A_1 r^{-2} - B_1 h(K_1 r) - B_2 h(K_2 r), \tag{B 13a}$$

$$g_1^\infty = mA_1 r^{-3} + A_2 r^{-1} h(kr) + \sum_{j=1}^{2} M_j B_j K_j [(K_j r)^{-1} h(K_j r) + h'(K_j r)], \tag{B 13b}$$

$$g_2^\infty = -3mA_1 r^{-3} + A_2 k[(kr)^{-1} h(kr) - h'(kr)]$$
$$+ \sum_{j=1}^{2} M_j B_j K_j [(K_j r)^{-1} h(K_j r) - h'(K_j r)], \tag{B 13c}$$

where the superscript '∞' denotes far-field asymptotic solutions. Similar to the numerical calculation of electrophoretic mobilities in Newtonian electrolytes, the foregoing far-field asymptotic solutions each differ from their exact solution by a multiplicative constant. Therefore, the boundary conditions at $r = r_{max}$ for the numerical computation of $f_{,r}(r)$, $g_1(r)$ and $g_2(r)$ are

$$f_{,r} - (f_{,r}^\infty / f_{,rr}^\infty) f_{,rr} = 0, \tag{B 14a}$$

$$f_{,rr} - (f_{,rr}^\infty / f_{,rrr}^\infty) f_{,rrr} = 0, \tag{B 14b}$$

$$g_1 - (g_1^\infty / g_{1,r}^\infty) g_{1,r} = 0, \tag{B 14c}$$

$$g_2 - (g_2^\infty / g_{2,r}^\infty) g_{2,r} = 0, \tag{B 14d}$$

and the asymptotic coefficient

$$C^X = A_1 f_{,r}(r_{max}) / f_{,r}^\infty(r_{max}) \text{ as } r_{max} \to \infty. \tag{B 15}$$

Appendix C. Far-field asymptotics for incompressible hydrogel skeletons

The combined fluid and $O(1)$ polymer equations of motion as $r \to \infty$ are

$$\nabla^2 \begin{pmatrix} \boldsymbol{u} \\ \boldsymbol{v}_0 \end{pmatrix} + \nabla \begin{pmatrix} -\eta^{-1} p \\ \nabla \cdot \boldsymbol{v}_1 \end{pmatrix} + \boldsymbol{M} \begin{pmatrix} \boldsymbol{u} \\ \boldsymbol{v}_0 \end{pmatrix} = \boldsymbol{0}, \tag{C 1}$$

where $\boldsymbol{M}$ is defined in (A 8). Diagonalizing $\boldsymbol{M}$ according to (A 9) and left-multiplying by $\boldsymbol{R}^{-1}$, which is defined in (A 9), yield two decoupled equations

$$\nabla^2 \boldsymbol{w}_j + \nabla q_j + \lambda_1 \boldsymbol{w}_j = 0 \ (j = 1, 2), \tag{C 2}$$

where

$$\begin{pmatrix} \boldsymbol{w}_1 \\ \boldsymbol{w}_2 \end{pmatrix} = \boldsymbol{R}^{-1} \begin{pmatrix} \boldsymbol{u} \\ \boldsymbol{v}_0 \end{pmatrix} \text{ and } \begin{pmatrix} q_1 \\ q_2 \end{pmatrix} = \boldsymbol{R}^{-1} \begin{pmatrix} -\eta^{-1} p \\ \nabla \cdot \boldsymbol{v}_1 \end{pmatrix}. \tag{C 3}$$

An incompressible fluid and polymer skeleton require $\nabla \cdot \boldsymbol{w}_j = 0$ $(j = 1, 2)$, so the solutions are

$$\boldsymbol{w}_j = \nabla \Phi_j + \nabla \times \boldsymbol{\Psi}_j + \boldsymbol{W}_j \ (j = 1, 2), \tag{C 4}$$

where Φ_j are scalar potentials; $\boldsymbol{\Psi}_j = \Psi_j \boldsymbol{e}_\phi$ are vector potentials; and

$$\begin{pmatrix} \boldsymbol{W}_1 \\ \boldsymbol{W}_2 \end{pmatrix} = \boldsymbol{R}^{-1} \begin{pmatrix} -i\omega Y \\ Y \end{pmatrix}. \tag{C 5}$$

Substituting the relations above into (C 2) and taking the curl yields

$$\nabla^2 \boldsymbol{\Psi}_j + \lambda_j \boldsymbol{\Psi}_j = 0 \ (j = 1, 2), \tag{C 6}$$

and incompressibility requires $\nabla^2 \Phi_i = 0$, so

$$\Phi_j = A'_j r^{-2} Y \cos\theta, \tag{C 7a}$$
$$\Psi_j = B'_j h(K_j r) Y \sin\theta, \tag{C 7b}$$

where A'_j and B'_j ($j = 1, 2$) are constants to match the boundary conditions at $r = a$, and $K_j = \sqrt{\lambda_j}$ with $\text{Im}(K_j) > 0$ to ensure vanishing polymer displacement and fluid velocity as $r \to \infty$. The radial and tangential components of $\boldsymbol{w}_j = \nabla \times \nabla \times [h_j(r) Y] + \boldsymbol{W}_j$ are

$$w_{jr} = [-2A'_j r^{-3} + 2B'_j r^{-1} h(K_j r) + (W_j/X)] X \cos\theta, \tag{C 8a}$$
$$w_{j\theta} = \{A'_j r^{-3} + B'_j K_j [(K_j r)^{-1} h(K_j r) + h'(K_j r)] + (W_j/X)\}(-X \sin\theta). \tag{C 8b}$$

Matching at $r = r_{max}$ gives

$$h^\infty_{j,r} = A'_j r^{-2} - B'_j h(K_j r) \text{ as } r_{max} \to \infty, \tag{C 9}$$

where the four constants A'_j and B'_j ($j = 1, 2$) are obtained from the boundary conditions at $r = a$ with $X = Y$ as

$$\begin{pmatrix} h^\infty_{1,r}(a) \\ h^\infty_{2,r}(a) \end{pmatrix} = \boldsymbol{R}^{-1} \begin{pmatrix} -i\omega a/2 \\ a/2 \end{pmatrix} \tag{C 10a}$$

and

$$\begin{pmatrix} h^\infty_{1,rr}(a) \\ h^\infty_{2,rr}(a) \end{pmatrix} = \boldsymbol{R}^{-1} \begin{pmatrix} -i\omega/2 \\ 1/2 \end{pmatrix}. \tag{C 10b}$$

Finally, the far-field boundary conditions for h_j at $r = r_{max}$ are

$$h_{j,r} - (h^\infty_{j,r}/h^\infty_{j,rr}) h_{j,rr} = 0 \text{ and } h_{j,rr} - (h^\infty_{j,rr}/h^\infty_{j,rrr}) h_{j,rrr} = 0 \ (j = 1, 2), \tag{C 11}$$

and the asymptotic coefficient

$$C^X = \sum_{j=1}^2 R_{1j} A'_j h_{j,r}(r_{max})/h^\infty_{j,r}(r_{max}) \text{ as } r_{max} \to \infty, \tag{C 12}$$

where R_{11} and R_{12} are elements of $\boldsymbol{R}$.

Appendix D. Point-force representation of a particle in an uncharged hydrogel matrix

Here we relate the net force on a spherical colloid in an uncharged hydrogel to the strength of a point force that produces the same far-field disturbances. The particle undergoes harmonic translation in an otherwise stationary hydrogel. The strength of the point force is obtained from reciprocal relations similar to Hill *et al.* (2003a). However, in addition to the Lorentz reciprocal relation for fluid in a domain S (Kim & Karrila 1991),

$$\int_{\partial S} (\boldsymbol{u}' \cdot \boldsymbol{T}^f - \boldsymbol{u} \cdot \boldsymbol{T}^{f'}) \cdot \hat{\boldsymbol{n}} \, \mathrm{d}A = \int_S (\boldsymbol{u}' \cdot \nabla \cdot \boldsymbol{T}^f - \boldsymbol{u} \cdot \nabla \cdot \boldsymbol{T}^{f'}) \, \mathrm{d}V, \tag{D 1}$$

a similar reciprocal relation, known in solid mechanics as the Betty theorem (Barber 2003), is required. This is

$$\int_{\partial S} (\mu' \boldsymbol{v}' \cdot \boldsymbol{T}^e - \mu \boldsymbol{v} \cdot \boldsymbol{T}^{e'}) \cdot \hat{\boldsymbol{n}} \, dA = \int_S (\mu' \boldsymbol{v}' \cdot \boldsymbol{\nabla} \cdot \boldsymbol{T}^e - \mu \boldsymbol{v} \cdot \boldsymbol{\nabla} \cdot \boldsymbol{T}^{e'}) \, dV, \qquad (D\,2)$$

provided $\lambda = \lambda'$.

Consider a large domain Ω with boundary $\partial\Omega$ and outward unit normal $\hat{\boldsymbol{n}}$ that encloses an oscillating sphere centred at position $\boldsymbol{r}_1$ with radius a (system 1) and a fixed point force centred at position $\boldsymbol{r}_2$ (system 2). Note that $|\boldsymbol{r}_1 - \boldsymbol{r}_2| \gg a + \kappa^{-1}$. Furthermore, the sphere occupies volume Ω_1 and undergoes oscillatory translation with velocity $-\mathrm{i}\omega \boldsymbol{Z}$. The corresponding surface and outward unit normal are denoted $\partial\Omega_1$ and $\hat{\boldsymbol{n}}_1$, respectively.

The divergence of elastic and hydrodynamic stresses for system 1 ($\boldsymbol{\nabla} \cdot \boldsymbol{T}_1^f$ and $\boldsymbol{\nabla} \cdot \boldsymbol{T}_1^e$) are given by (3.20$b$) and (3.20$c$), respectively. For system 2,

$$\boldsymbol{\nabla} \cdot \boldsymbol{T}_2^f = \eta \nabla^2 \boldsymbol{u}_2 - \boldsymbol{\nabla} p_2 = -\mathrm{i}\omega \rho_f \boldsymbol{u}_2 + \eta \ell^{-2}(\boldsymbol{u}_2 + \mathrm{i}\omega \boldsymbol{v}_2) + \boldsymbol{F}^f \delta(\boldsymbol{r}_2), \qquad (D\,3a)$$

$$\boldsymbol{\nabla} \cdot \boldsymbol{T}_2^e = \mu \nabla^2 \boldsymbol{v}_2 + (\lambda + \mu) \boldsymbol{\nabla}(\boldsymbol{\nabla} \cdot \boldsymbol{v}_2) = \boldsymbol{F}^e \delta(\boldsymbol{r}_2) - \eta \ell^{-2}(\boldsymbol{u}_2 + \mathrm{i}\omega \boldsymbol{v}_2), \qquad (D\,3b)$$

where $\delta(\boldsymbol{r})$ is the Dirac-delta function and $\boldsymbol{F}^f$ and $\boldsymbol{F}^e$ are the point forces exerted on the fluid and elastic medium, respectively.

Applying the Lorentz reciprocal relation to the volume enclosed by $\partial\Omega_1$ and $\partial\Omega$ gives

$$\int_{\partial\Omega} \left(\boldsymbol{u}_1 \cdot \boldsymbol{T}_2^f - \boldsymbol{u}_2 \cdot \boldsymbol{T}_1^f\right) \cdot \hat{\boldsymbol{n}} \, dA - \int_{\partial\Omega_1} \left(\boldsymbol{u}_1 \cdot \boldsymbol{T}_2^f - \boldsymbol{u}_2 \cdot \boldsymbol{T}_1^f\right) \cdot \hat{\boldsymbol{n}}_1 \, dA$$

$$= \int_{\Omega - \Omega_1} \left(\boldsymbol{u}_1 \cdot \boldsymbol{\nabla} \cdot \boldsymbol{T}_2^f - \boldsymbol{u}_2 \cdot \boldsymbol{\nabla} \cdot \boldsymbol{T}_1^f\right) dV. \quad (D\,4)$$

Because $\boldsymbol{u} \sim r^{-3}$ as $r \to \infty$, the integral over $\partial\Omega$ on the left-hand side of (D\,4) vanishes when Ω is sufficiently large. Therefore, substituting (3.20b) and (D\,3a) into (D\,4) gives

$$-\int_{\partial\Omega_1} \left(\boldsymbol{u}_1 \cdot \boldsymbol{T}_2^f - \boldsymbol{u}_2 \cdot \boldsymbol{T}_1^f\right) \cdot \hat{\boldsymbol{n}}_1 \, dA = \boldsymbol{u}_1(\boldsymbol{r}_2) \cdot \boldsymbol{F}^f$$

$$+ \int_{\Omega - \Omega_1} \left[\mathrm{i}\omega \eta \ell^{-2}\left(\boldsymbol{u}_1 \cdot \boldsymbol{v}_2 - \boldsymbol{u}_2 \cdot \boldsymbol{v}_1\right) + \boldsymbol{u}_2 \cdot \boldsymbol{\nabla} \cdot \boldsymbol{T}_1^m\right] dV. \quad (D\,5)$$

Inside the particle, $\boldsymbol{u}_1 = -\mathrm{i}\omega \boldsymbol{Z}$, and since $|\boldsymbol{r}_1 - \boldsymbol{r}_2| \gg a + \kappa^{-1}$, $\boldsymbol{u}_2(|\boldsymbol{x} - \boldsymbol{r}_1| \leqslant a)$ can be considered constant. Therefore, applying Gauss's divergence theorem to the integral over $\partial\Omega_1$ on the left-hand side of (D\,5) gives

$$\int_{\partial\Omega_1} \left(\boldsymbol{u}_1 \cdot \boldsymbol{T}_2^f - \boldsymbol{u}_2 \cdot \boldsymbol{T}_1^f\right) \cdot \hat{\boldsymbol{n}}_1 \, dA = -\mathrm{i}\omega \boldsymbol{Z} \cdot \int_{\Omega_1} \boldsymbol{\nabla} \cdot \boldsymbol{T}_2^f \, dV - \boldsymbol{u}_2(\boldsymbol{r}_1) \cdot \int_{\partial\Omega_1} \boldsymbol{T}_1^f \cdot \hat{\boldsymbol{n}}_1 \, dA$$

$$= -\boldsymbol{u}_2(\boldsymbol{r}_1) \cdot \left[\omega^2 \rho_f V_p \boldsymbol{Z} + \int_{\partial\Omega_1} \boldsymbol{T}_1^f \cdot \hat{\boldsymbol{n}}_1 \, dA\right], \qquad (D\,6)$$

where V_p is the particle volume. Substituting (D\,6) into (D\,5) gives

$$\boldsymbol{F}^f \cdot \boldsymbol{u}_1(\boldsymbol{r}_2) = \boldsymbol{u}_2(\boldsymbol{r}_1) \cdot \left[\omega^2 \rho_f V_p \boldsymbol{Z} + \int_{\partial\Omega_1} \boldsymbol{T}_1^f \cdot \hat{\boldsymbol{n}}_1 \, dA\right]$$

$$- \int_{\Omega - \Omega_1} [\mathrm{i}\omega \eta \ell^{-2}(\boldsymbol{u}_1 \cdot \boldsymbol{v}_2 - \boldsymbol{u}_2 \cdot \boldsymbol{v}_1) + \boldsymbol{u}_2 \cdot \boldsymbol{\nabla} \cdot \boldsymbol{T}_1^m] \, dV. \qquad (D\,7)$$

Similarly, for the elastic displacements, applying the same procedure as above, but with the Betty theorem, yields

$$\boldsymbol{F}^e \cdot \boldsymbol{v}_1(\boldsymbol{r}_2) = \boldsymbol{v}_2(\boldsymbol{r}_1) \cdot \int_{\partial\Omega_1} \boldsymbol{T}_1^e \cdot \hat{\boldsymbol{n}}_1 \, \mathrm{d}A - \int_{\Omega-\Omega_1} \eta\ell^{-2}(\boldsymbol{u}_1 \cdot \boldsymbol{v}_2 - \boldsymbol{u}_2 \cdot \boldsymbol{v}_1) \, \mathrm{d}V, \qquad (\mathrm{D}\,8)$$

where $\boldsymbol{v}_2(|\boldsymbol{x} - \boldsymbol{r}_1| \leqslant a)$ may be considered constant.

Again, since $\boldsymbol{u}_1(\boldsymbol{r}_2) = -\mathrm{i}\omega\boldsymbol{v}_1(\boldsymbol{r}_2)$ and $\boldsymbol{u}_2(\boldsymbol{r}_1) = -\mathrm{i}\omega\boldsymbol{v}_2(\boldsymbol{r}_1)$, multiplying (D 8) by $-\mathrm{i}\omega$ and adding (D 7) gives

$$\boldsymbol{F} \cdot \boldsymbol{u}_1(\boldsymbol{r}_2) = \boldsymbol{u}_2(\boldsymbol{r}_1) \cdot \left[\omega^2 \rho_f V_p \boldsymbol{Z} + \int_{\partial\Omega_1} (\boldsymbol{T}_1^f + \boldsymbol{T}_1^e) \cdot \hat{\boldsymbol{n}}_1 \, \mathrm{d}A \right] - \int_{\Omega-\Omega_1} \boldsymbol{u}_2 \cdot \nabla \cdot \boldsymbol{T}_1^m \, \mathrm{d}V, \quad (\mathrm{D}\,9)$$

where $\boldsymbol{F} = \boldsymbol{F}^e + \boldsymbol{F}^f$ is the total point force. Note that the volume integral on the right-hand side of (D 9) can be factored to give

$$\int_{\Omega-\Omega_1} \boldsymbol{u}_2 \cdot \nabla \cdot \boldsymbol{T}_1^m \, \mathrm{d}V = -\boldsymbol{u}_2(\boldsymbol{r}_1) \cdot \int_{\partial\Omega_1} \boldsymbol{T}_1^m \cdot \hat{\boldsymbol{n}}_1 \, \mathrm{d}A \qquad (\mathrm{D}\,10)$$

because $\nabla \cdot \boldsymbol{T}^m$ is exponentially small when $|\boldsymbol{x} - \boldsymbol{r}_1| \gg a + \kappa^{-1}$, and $\boldsymbol{u}_2$ can be considered constant where $\nabla \cdot \boldsymbol{T}^m$ is finite.

Substituting (D 10) into (D 9) yields

$$\boldsymbol{F} = \omega^2 \rho_f V_p \boldsymbol{Z} + \int_{\partial\Omega_1} \left(\boldsymbol{T}_1^e + \boldsymbol{T}_1^f + \boldsymbol{T}_1^m \right) \cdot \hat{\boldsymbol{n}}_1 \, \mathrm{d}A. \qquad (\mathrm{D}\,11)$$

The integral over $\partial\Omega_1$ on the left-hand side of (D 11) is the total force on the sphere, which according to Newton's second law must equal the acceleration of its mass $-V_p \rho_p \omega^2 \boldsymbol{Z}$, so the strength of the point force is

$$\boldsymbol{F} = \omega^2 V_p \boldsymbol{Z}(\rho_f - \rho_p). \qquad (\mathrm{D}\,12)$$

In other words, similar to bare particles (Mangelsdorf & White 1992) and particles with polymer coatings (Hill *et al.* 2003*a*) dispersed in Newtonian electrolytes, the acceleration of the mass of fluid displaced by a finite-sized inclusion in a hydrogel must be added to the force on a point particle producing the same far-field fluid velocity and polymer displacement disturbances. Note that the foregoing analysis neglects the mass of the polymer.

Appendix E. Numerical solution of the field equations

The field equations are solved according to the methodology outlined in § 3. First, the Poisson–Boltzmann equation is efficiently solved using the adaptive mesh algorithm developed by Hill *et al.* (2003*a*), and then various equilibrium quantities and their derivatives are computed. Next, the linearly perturbed equations are solved. Before this calculation, the equations are transformed to simplify the numerics. Matrix algebra and eigenvalue calculations involved in the transformations are performed using BLAS and LAPACK routines (Anderson *et al.* 1999). Independent computational strategies are adopted for calculating the linearized perturbations for incompressible and compressible hydrogel skeletons. Asymptotic coefficients and physical quantities are then constructed from the numerical solutions. The following discusses in further detail how the perturbed problems are solved.

For incompressible skeletons, the perturbed equations are transformed to the decoupled forms outlined in Appendix A, and the resulting differential equations

are discretized using a second-order central difference scheme and solved using a banded matrix solver. Solutions are then iteratively improved using a moving mesh method based on the methodology of Hill *et al.* (2003*a*). When the solution has converged, asymptotic coefficients from the far-field asymptotic analysis undertaken in Appendix B are obtained. The far-field solution is facilitated using LAPACK. Our program to compute the response for incompressible skeletons is written entirely in C.

For compressible skeletons, the perturbed solutions oscillate in space with several wavelengths, e.g. the construction of the fluid velocity and polymer displacement in §2 involves three wavelengths. The second-order central difference scheme with the moving mesh method of Hill *et al.* (2003*a*) does not converge. We therefore modified a general-purpose boundary value problem software package TWPBVPL (Cash & Mazzia 2006), which solves the differential equations using fourth-, sixth- and eighth-order methods with hybrid mesh selection, to solve the linearly perturbed problem. The second-order ordinary differential equations (ODEs) presented in §3.2, i.e. (3.6) and (3.8)–(3.11), are arranged as a set of first-order ODEs,

$$\boldsymbol{x}_{,r} = \boldsymbol{C} \cdot \boldsymbol{x} + \boldsymbol{q}, \tag{E 1}$$

where $\boldsymbol{x} = [\hat{n}_1, \ \hat{n}_{1,r}, \ldots, \ \hat{n}_N, \ \hat{n}_{N,r}, \ \hat{\psi}, \ \hat{\psi}_{,r}, \ f_{,r}, \ f_{,rr}, \ f_{,rrr}, \ f_{,rrrr}, \ g_1, \ g_{1,r}, \ g_2, \ g_{2,r}]^T$ is a vector of unknown functions; $\boldsymbol{C}$ is a coefficient matrix; and $\boldsymbol{q}$ is a vector. Note that $\boldsymbol{x}$, $\boldsymbol{C}$ and $\boldsymbol{q}$ all depend on radial position r. To convert $\hat{n}_j$ ($j = 1, 2, \ldots, N$) and $\hat{\psi}$ to χ_k ($k = 1, 2, \ldots, N+1$) in $\boldsymbol{x}$, we introduce a square transformation matrix

$$\boldsymbol{T} = \begin{pmatrix} \tilde{\boldsymbol{Q}}^{-1} & 0 \\ 0 & \boldsymbol{I} \end{pmatrix} \tag{E 2}$$

and a transformed vector of unknowns

$$\boldsymbol{y} = \boldsymbol{T} \cdot \boldsymbol{x}. \tag{E 3}$$

Here, $\boldsymbol{Q}$ is given in (B 5), and the tilde denotes a matrix augmentation operation that increases the size of an $n \times n$ matrix $\boldsymbol{M}$ (with elements M_{ij}) to a $2n \times 2n$ augmented matrix,

$$\tilde{\boldsymbol{M}} = \begin{pmatrix} M_{11} & 0 & M_{12} & 0 & \ldots & M_{1n} & 0 \\ 0 & M_{11} & 0 & M_{12} & \ldots & 0 & M_{1n} \\ \vdots & \vdots & \vdots & \vdots & \ddots & \vdots & \vdots \\ M_{n1} & 0 & M_{n2} & 0 & \ldots & M_{nn} & 0 \\ 0 & M_{n1} & 0 & M_{n2} & \ldots & 0 & M_{nn} \end{pmatrix}. \tag{E 4}$$

Equation (E 1) is then transformed to

$$\boldsymbol{y}_{,r} = (\boldsymbol{T}\boldsymbol{C}\boldsymbol{T}^{-1}) \cdot \boldsymbol{y} + \boldsymbol{T} \cdot \boldsymbol{q}, \tag{E 5}$$

where the far-field boundary conditions at $r = r_{max}$ given in Appendix B can be directly applied. The original boundary conditions at the particle surface $r = a$ in matrix form

$$\boldsymbol{B} \cdot \boldsymbol{x} = \boldsymbol{\beta} \tag{E 6}$$

are transformed to

$$(\boldsymbol{B}\boldsymbol{T}^{-1}) \cdot \boldsymbol{y} = \boldsymbol{\beta}. \tag{E 7}$$

The transformed equation (E 5), together with their boundary conditions, i.e. (E 7) as boundary conditions at $r = a$ and far-field boundary conditions presented in Appendix B at $r = r_{max}$, are first solved with a second-order central difference scheme (Ascher, Mattheij & Russell 1988) on the non-uniform mesh of the equilibrium solution. With this initial guess, TWPBVPL is used to calculate y by adjusting the mesh and applying higher-order methods. The far-field boundary conditions are calculated using multiple precision packages GMP (Granlund 2007), MPFR (Fousse *et al.* 2007) and MPC (Enge *et al.* 2007) to avoid round-off errors, and various matrix operations are performed using LAPACK and BLAS. When the error tolerance or the maximum number of iterations is achieved, asymptotic coefficients are extracted. The program combines codes written in C and FORTRAN.

REFERENCES

AHUALLI, S., DELGADO, A. V., MIKLAVCIC, S. J. & WHITE, L. R. 2006 Dynamic electrophoretic mobility of concentrated dispersions of spherical colloidal particle. On the consistent use of the cell model. *Langmuir* **22**, 7041–7051.

ALLERSMA, M. W., GITTES, F., DE CASTRO, M. J., STEWART, R. J. & SCHMIDT, C. F. 1998 Two-dimensional tracking of ncd motility by back focal plane interferometry. *Biophys. J.* **74**, 1074–1085.

ANDERSON, E., BAI, Z., BISCHOF, C., BLACKFORD, S., DEMMEL, J., DONGARRA, J., DU CROZ, J., GREENBAUM, A., HAMMARLING, S., MCKENNEY, A. & SORENSEN, D. 1999 *LAPACK Users' Guide*, 3rd edn. Society for Industrial and Applied Mathematics.

ASCHER, U. M., MATTHEIJ, R. M. M. & RUSSELL, R. D. 1988 *Numerical Solution of Boundary Value Problems for Ordinary Differential Equations*. Prentice Hall.

BARBER, J. R. 2003 *Elasticity*, 2nd edn. Springer.

BARNDL, F., SOMMER, F. & GOEPFERICH, A. 2007 Rational design of hydrogels for tissue engineering: impact of physical factors on cell behaviour. *Biomaterials* **28** (2), 134–146.

BERG-SØRENSEN, K. & FLYVBJERG, H. 2004 Power spectrum analysis for optical tweezers. *Rev. Sci. Inst.* **75**, 594–612.

BREUER, K. (ed.) 2005 *Microscale Diagnostic Techniques*. Springer.

BRINKMAN, H. C. 1947 A calculation of the viscous force exerted by a flowing fluid on a dense swarm of particles. *Appl. Sci. Res.* A **1**, 27–34.

CASH, J. R. & MAZZIA, F. 2006 Hybrid mesh selection algorithms based on conditioning for two-point boundary value problems. *J. Numer. Anal. Indust. Appl. Math.* **1**, 81–90.

CHATERJI, S., KWON, I. K. & PARK, K. 2007 Smart polymeric gels: redefining the limits of biomedical devices. *Prog. Polym. Sci.* **32**, 1083–1122.

CHUNG, Y.-I., AHN, K.-M., JEON, S.-H., LEE, S.-Y., LEE, J.-H. & TAE, G. 2007 Enhanced bone regeneration with BMP-2 loaded function nanoparticle–hydrogel complex. *J. Control. Release* **121**, 91–99.

CICUTA, P. & DONALD, A. M. 2007 Microrheology: a review of the method and applications. *Soft Matt.* **3**, 1449–1455.

CROCKER, J. C., VALENTINE, M. T. & WEEKS, E. R. 2000 Two-point microrheology of inhomogeneous soft materials. *Phys. Rev. Lett.* **85** (4), 888–891.

DAYTON, P. A. & FERRARA, K. W. 2002 Targeted imaging using ultrasound. *J. Magnet. Reson. Imag.* **16**, 362–377.

DELACEY, E. H. B. & WHITE, L. R. 1981 Dielectric response and conductivity of dilute suspensions of colloidal particles. *J. Chem. Soc., Faraday Trans.* **77**, 2007–2039.

DRURY, J. L. & MOONEY, D. J. 2003 Hydrogels for tissue engineering: scaffold design variables and applications. *Biomaterials* **24**, 4337–4351.

EDDINGTON, D. T. & BEEBE, D. J. 2004 Flow control with hydrogels. *Adv. Drug Deliv. Rev.* **56**, 199–210.

ENGE, A., PÉLISSIER, P. & ZIMMERMANN, P. 2007 *MPC: Multiple Precision Complex Library*. INRIA.

Fousse, L., Hanrot, G., Lefèvre, V., Pélissier, P. & Zimmermann, P. 2007 MPFR: A multiple-precision binary floating-point library with correct rounding. *ACM T. Math. Software* **33**, 13.

Galneder, R., Kahl, V., Arbuzova, A., Rebecchi, M., Radler, J. O. & McLaughlin, S. 2001 Microelectrophoresis of a bilayer-coated silica bead in an optical trap: application to enzymology. *Biophys. J.* **80**, 2298–2309.

Geissler, E. & Hecht, A. M. 1980 The Poisson ratio in polymer gels. *Macromolecules* **13**, 1276–1280.

Geissler, E. & Hecht, A. M. 1981 The Poisson ratio in polymer gel. 2. *Macromolecules* **14**, 185–188.

Gibb, S. E. & Hunter, R. J. 2000 Dynamic mobility of colloidal particles with thick double layers. *J. Colloid Interface Sci.* **224**, 99–111.

Granlund, T. 2007 *GNU MP: The GNU Multiple Precision Arithmetic Library*, 4th edn.

Hill, R. J. 2006a Electric-field-induced force on a charged spherical colloid embedded in an electrolyte-saturated Brinkman medium. *Phys. Fluids* **18**, 043103.

Hill, R. J. 2006b Transport in polymer-gel composites: theoretical methodology and response to an electric field. *J. Fluid Mech.* **551**, 405–433.

Hill, R. J. 2007 Electric-field-enhanced transport in polyacrylamide hydrogel nanocomposites. *J. Colloid Interface Sci.* **316**, 635–644.

Hill, R. J. & Ostoja-Starzewski, M. 2008 Electric-field-induced displacement of a charged spherical colloid embedded in an elastic Brinkman medium. *Phys. Rev. E* **77**, 011404.

Hill, R. J., Saville, D. A. & Russel, W. B. 2003a Electrophoresis of spherical polymer-coated colloidal particles. *J. Colloid Interface Sci.* **258**, 56–74.

Hill, R. J., Saville, D. A. & Russel, W. B. 2003b High-frequency dielectric relaxation of spherical colloidal particles. *Phys. Chem. Chem. Phys.* **5**, 911–915.

Hunter, R. J. 1998 Recent developments in the electroacoustic characterization of colloidal suspensions and emulsions. *Colloids Surf.* A **141**, 37–65.

Hunter, R. J. 2001 *Foundations of Colloid Science*, 2nd edn. Oxford University Press.

Hunter, R. J. & O'Brien, R. W. 1997 Electroacoustic characterization of colloids with unusual particle properties. *Colloids Surf.* A **126**, 123–128.

Khademhosseini, A. & Langer, R. 2007 Microengineered hydrogels for tissue engineering. *Biomaterials* **28**, 5087–5092.

Kim, J. J. & Park, K. 1998 Smart hydrogels for bioseparation. *Bioseparation* **7**, 177–184.

Kim, S. & Karrila, S. J. 1991 *Microhydrodynamics: Principles and Selected Applications*. Butterworth-Heinemann.

Kimura, Y. & Mizuno, D. 2007 Microrheology of a swollen lyotropic lamellar phase. *Mol. Cryst. Liq. Cryst.* **478**, 3–13.

Kizilay, M. Y. & Okay, O. 2003 Effect of hydrolysis on spatial inhomogeneity in poly(acrylamide) gels of various crosslink densities. *Polymer* **44**, 5239–5250.

Lamb, H. 1945 *Hydrodynamics*, 6th edn. Dover

Landau, L. D. & Lifshitz, E. M. 1987 *Fluid Mechanics*. Pergamon.

Larsen, T. H. & Furst, E. M. 2008 Microrheology of the liquid–solid transition during gelation. *Phys. Rev. Lett.* **100** (14), 146001.

Larson, R. G. 1999 *The Structure and Rheology of Complex Fluids*. Oxford University Press.

Levine, A. J. & Lubensky, T. C. 2000 One- and two-particle microrheology. *Phys. Rev. Lett.* **85**, 1774–1777.

Levine, A. J. & Lubensky, T. C. 2001 Response function of a sphere in a viscoelastic two-fluid medium. *Phys. Rev. E* **63**, 041510.

Lin, C.-C. & Netters, A. T. 2006 Hydrogels in controlled release formulations: network design and mathematical modelling. *Adv. Drug Deliv. Rev.* **58**, 1379–1408.

Liu, J., Levine, A. L., Mattoon, J. S., Yamaguchi, M., Lee, R. J., Pan, X. L. & Rosol, T. J. 2006 Nanoparticles as image enhancing agents for ultrasonography. *Phys. Med. Biol.* **51**, 2179–2189.

Loo, C., Lowery, A., Halas, N., West, J. & Drezek, R. 2005 Immunotargeted nanoshells for integrated cancer imaging and therapy. *Nano Lett.* **5**, 709–711.

Lyklema, J. 1995 *Fundamentals of Interface and Colloid Science. II. Solid–Liquid Interfaces*. Academic.

MacKintosh, F. C. & Schmidt, C. F. 1999 Microrheology. *Curr. Opin. Colloid Interface Sci.* **4**, 300–307.

MacRobert, T. M. 1967 *Spherical Harmonics: An Elementary Treatise on Harmonic Functions, with Applications*, 3rd edn. Pergamon.

Mangelsdorf, C. S. & White, L. R. 1992 Electrophoretic mobility of a spherical colloidal particle in an oscillating electric field. *J. Chem. Soc., Faraday Trans.* **88**, 3567–3581.

Markov, M. G. 2005 Propagation of longitudinal elastic waves in a fluid-saturated porous medium with spherical inclusions. *Acoust. Phys.* **51**, S115–S121.

Masliyah, J. H. & Bhattacharjee, S. 2006 *Electrokinetic and Colloid Transport Phenomena*. Wiley Interscience.

Mason, T. & Weitz, D. 1995 Optical measurements of frequency-dependent linear viscoelastic moduli of complex fluids. *Phys. Rev. Lett.* **74** (7), 1250–1253.

Matos, M., White, L. R. & Tilton, R. D. 2008 Enhanced mixing in polyacrylamide gels containing embedded silica nanoparticles as internal electro-osmotic pumps. *Colloids Surf.* B **61** (2), 262–269.

Matos, M. A., White, L. R. & Tilton, R. D. 2006 Electroosmotically enhanced mass transfer through polyacrylamide gels. *J. Colloid Interface Sci.* **300**, 429–436.

Mizuno, D., Head, D. A., MacKintosh, F. C. & Schmidt, C. F. 2008 Active and passive microrheology in equilibrium and nonequilibrium systems. *Macromolecules* **41** (19), 7194–7202.

Mizuno, D., Kimura, Y. & Hayakawa, R. 2000 Dynamic electrophoretic mobility of colloidal particles measured by the newly developed method of quasi-elastic light scattering in a sinusoidal electric field. *Langmuir* **16**, 9547–9554.

Mizuno, D., Kimura, Y. & Hayakawa, R. 2001 Electrophoretic microrheology in a dilute lamellar phase of a nonionic surfactant. *Phys. Rev. Lett.* **87**, 088104.

Mizuno, D., Kimura, Y. & Hayakawa, R. 2004 Electrophoretic microrheology of a dilute lamellar phase: relaxation mechanisms in frequency-dependent mobility of nanometre-sized particles between soft membranes. *Phys. Rev.* E **70**, 011509.

Mohammadi, A. & Hill, R. J. 2009 Steady electrical and microrheological response functions for uncharged colloidal inclusions in polyelectrolyte hydrogels. *Proc. R. Soc. A*, (submitted).

Nägele, G. 2003 Viscoelasticity and diffusional properties of colloidal model dispersions. *J. Phys., Condens. Matt.* **15** (1), S407–S414.

O'Brien, R. W. 1979 A method for the calculation of the effective transport properties of suspensions of interacting particles. *J. Fluid Mech.* **91**, 17–39.

O'Brien, R. W. 1986 The high frequency dielectric dispersion of a colloid. *J. Colloid Interface Sci.* **113**, 81–93.

O'Brien, R. W. 1988 Electro-acoustic effects in a dilute suspension of spherical particles. *J. Fluid Mech.* **190**, 71–86.

O'Brien, R. W. 1990 The electroacoustic equations for a colloidal suspension. *J. Fluid Mech.* **212**, 81–93.

O'Brien, R. W., Jones, A. & Rowlands, W. N. 2003 A new formula for the dynamic mobility in a concentrated colloid. *Colloids Surf.* A **218**, 89–101.

O'Brien, R. W. & White, L. R. 1978 Electrophoretic mobility of a spherical colloidal particle. *J. Chem. Soc., Faraday Trans.* **74**, 1607–1626.

Oestreicher, H. L. 1951 Field and impedance of an oscillating sphere in a viscoelastic medium with an application to biophysics. *J. Acoust. Soc. Am.* **23**, 707–714.

O'Konski, C. T. 1960 Electric properties of macromolecules. Part V. Theory of ionic polarization in polyelectrolytes. *J. Phys. Chem.* **64**, 605–619.

Peppas, N. A., Bures, P., Leobandung, W. & Ichikawa, H. 2000 Hydrogels in pharmaceutical formulations. *Eur. J. Pharm. Biopharm.* **50**, 27–46.

Peppas, N. A., Hilt, J. Z., Khademhosseini, A. & Langer, R. 2006 Hydrogels in biology and medicine: from molecular principles to bionanotechnology. *Adv. Mater.* **18**, 1345–1360.

Pine, D. J., Weitz, D. A., Chaikin, P. M. & Herbolzheimer, E. 1988 Diffusing wave spectroscopy. *Phys. Rev. Lett.* **61**, 1134–1137.

Pozrikidis, C. 1996 *Introduction to Theoretical and Computational Fluid Dynamics*. Oxford University Press.

Preston, M. A., Kornbrekke, R. & White, L. R. 2005 Determination of the dynamic electrophoretic mobility of a spherical colloidal particle through a novel numerical solution of the electrokinetic equations. *Langmuir* **21**, 9832–9842.

Qiu, Y. & Park, K. 2001 Environment-sensitive hydrogels for drug delivery. *Adv. Drug Deliv. Rev.* **53**, 321–339.

Rider, P. F. & O'Brien, R. W. 1993 The dynamic mobility of particles in a non-dilute suspension. *J. Fluid Mech.* **257**, 607–636.

Russel, W. B., Schowalter, W. R. & Saville, D. A. 1989 *Colloidal Dispersions*. Cambridge University Press.

Sato, J. & Breedveld, V. 2006 Transient rheology of solvent-responsive complex fluids by integrating microrheology and microfluidics. *J. Rheology* **50** (1), 1–19.

Schnurr, B., Gittes, F., MacKintosh, F. C. & Schmidt, C. F. 1997 Determining microscopic viscoelasticity in flexible and semiflexible polymer networks from thermal fluctuations. *Macromolecules* **30**, 7781–7792.

Sershen, S. R., Mensing, G. A., Ng, M., Halas, N. J., Beebe, D. J. & West, J. L. 2005 Independent optical control of microfluidic valves formed from optomechanically responsive nanocomposite hydrogels. *Adv. Mater.* **17**, 1366–1368.

Shkel, I. A., Tsodikov, O. V. & Record Jr, M. T. 2000 Complete asymptotic solution of cylindrical and spherical Poisson–Boltzmann equations at experimental salt concentrations. *J. Phys. Chem.* B **104**, 5161–5170.

Speight, J. G. 2005 *Lange's Handbook of Chemistry*, 16th edn. McGraw-Hill.

Takigawa, T., Morino, Y., Urayama, K. & Masuda, T. 1996 Poisson's ratio of polyacrylamide (PAAm) gels. *Polym. Gels Networks* **4**, 1–5.

Takigawa, T., Yamawaki, T., Takahashi, K. & Masuda, T. 1997 Change in Young's modulus of poly(N-isopropylacrylamide) gels by volume phase transition. *Polym. Gels Networks* **5**, 585–589.

Temkin, L. & Leung, C. M. 1976 On the velocity of a rigid sphere in a sound wave. *J. Sound Vib.* **49**, 75–92.

Thévenot, C., Khoukh, A., Reynaud, S., Desbrières, J. & Grassl, B. 2007 Kinetic aspects, rheological properties and mechanoelectrical effects of hydrogels composed of polyacrylamide and polystyrene nanoparticles. *Soft Matt.* **3**, 437–447.

Valentine, M. T., Dewalt, L. E. & Ou-Yang, H. D. 1996 Forces on a colloidal particle in a polymer solution: a study using optical tweezers. *J. Phys., Condens. Matt.* **8**, 9477–9482.

Verwey, E. J. W. & Overbeek, J. T. G. 1948 *Theory of Stability of Lyophobic Colloids*. Elsevier.

Wang, K. L., Burban, J. H. & Cussler, E. L. 1993 Hydrogels as separation agents. *Adv. Polym. Sci.* **110**, 67–79.

Wang, M. & Hill, R. J. 2008 Electric-field-induced displacement of charged spherical colloids in compressible hydrogels. *Soft Matt.* **4**, 1048–1058.

Yamaguchi, N., Chae, E.-S., Zhang, L., Kiick, K. L. & Furst, E. M. 2005 Rheological characterization of polysaccharide-poly(ethylene glycol) star copolymer hydrogels. *Biomacromolecules* **6**, 1931–1940.

Yao, S. H., Hertzog, D. E., Zeng, S. L., Mikkelsen, J. C. & Santiago, J. G. 2003 Porous glass electro-osmotic pumps: design and experiments. *J. Colloid Interface Sci.* **268**, 143–153.

Yao, S. H. & Santiago, J. G. 2003 Porous glass electro-osmotic pumps: theory. *J. Colloid Interface Sci.* **268**, 133–142.

Ziemann, F., Radler, J. & Sackmann, E. 1994 Local measurement of viscoelastic moduli of entangled actin networks using an oscillating magnetic bead micro-rheometer. *Biophys. J.* **66**, 2210–2216.